J. Fluid Mech. (2018), *vol.* 850, *pp.* 336–369.
doi:10.1017/jfm.2018.442

A direct comparison of particle-resolved and point-particle methods in decaying turbulence

M. Mehrabadi[1,‡], J. A. K. Horwitz[2,‡], S. Subramaniam[3,†] and A. Mani[2]

[1]University of Illinois at Urbana-Champaign, Department of Aerospace Engineering, Urbana, IL 61820, USA

[2]Stanford University, Department of Mechanical Engineering, Stanford, CA 94305, USA

[3]Iowa State University, Department of Mechanical Engineering, Ames, IA 50010, USA

(Received 10 September 2017; revised 11 February 2018; accepted 9 May 2018; first published online 4 July 2018)

We use particle-resolved direct numerical simulation (PR-DNS) as a model-free physics-based numerical approach to validate particle acceleration modelling in gas-solid suspensions. To isolate the effect of the particle acceleration model, we focus on point-particle direct numerical simulation (PP-DNS) of a collision-free dilute suspension with solid-phase volume fraction $\phi = 0.001$ in a decaying isotropic turbulent particle-laden flow. The particle diameter d_p in the suspension is chosen to be the same as the initial Kolmogorov length scale η_0 ($d_p/\eta_0 = 1$) in order to overlap with the regime where PP-DNS is valid. We assess the point-particle acceleration model for two different particle Stokes numbers, $St_\eta = 1$ and 100. For the high Stokes number case, the Stokes drag model for particle acceleration under-predicts the true particle acceleration. In addition, second moment quantities which play key roles in the physical evolution of the gas–solid suspension are not correctly captured. Considering finite Reynolds number corrections to the acceleration model improves the prediction of the particle acceleration probability density function and second moment statistics of the point-particle model compared with the particle-resolved simulation. We also find that accounting for the undisturbed fluid velocity in the acceleration model can be of greater importance than using the most appropriate acceleration model for a given physical problem.

Key words: isotropic turbulence, particle/fluid flows, suspensions

1. Introduction

Turbulent flows containing solid particles are commonly found in nature. For example, the transport of air pollutants, volcanic ash and sandstorms occurring in atmospheric turbulence can significantly affect our daily lives. On the other hand, turbulent gas–solid flows are frequently encountered in industrial applications such as fluidized-bed combustion, fluid catalytic cracking, coal gasification and biomass energy generation (Fan, Marchisio & Fox 2004). Prediction of such systems requires understanding of the respective dynamics of the carrier and dispersed phases as well as how these dynamics couple.

† Email address for correspondence: shankar@iastate.edu

‡ Equally contributing first authors.

While the underlying dynamics of gas–solid flows is determined by the coupling of the dispersed and carrier phases, from a modelling perspective, it is often easier to neglect various degrees of physical coupling between the particles and the fluid as well as among the particles themselves. In zero-way coupling, particles are effectively massless and move as fluid tracers. In one-way coupling, particles have finite mass and experience a drag force owing to the surrounding fluid. However, the mass loading of particles is very small, such that the fluid is essentially unaware of the dispersed phase's presence. In contrast, in two-way coupled flows, the mass loading of particles is significant enough to cause measurable turbulence modification. In this regime, the fluid experiences an equal and opposite drag force owing to the presence of each dispersed phase element. Finally, in four-way coupled flows, the mean free path of particles is small enough, or the bulk volume fraction is large enough, for collisions to become important. For clarity, it should be noted that the notion of an 'n-way coupled' system is purely a 'modelling' simplification and to call a system one-way coupled, (where particles experience drag and the fluid feels nothing), for instance, is to say the physical system in question is expected to have little non-dimensional momentum or energy coupling. In reality, the correct 'physical' description of every particle-laden fluid is four-way coupled.

A popular numerical approach for gas–solid systems with particles smaller than the Kolmogorov length scale is the point-particle direct numerical simulation (PP-DNS) methodology. In this method, particles are tracked in a Lagrangian frame, whereas the continuum fluid phase is represented in a fixed Eulerian frame. Some of the seminal papers using point-particle methods include studies on particle dispersion (Riley & Patterson 1974; Squires & Eaton 1991*a*; Elghobashi & Truesdell 1992; Truesdell & Elghobashi 1994), particle-particle collision (Sundaram & Collins 1997; Reade & Collins 2000), settling (Wang & Maxey 1993; Frankel *et al.* 2016), and turbulence modification (Squires & Eaton 1990, 1991*b*; Elghobashi & Truesdell 1993; Boivin, Simonin & Squires 1998; Sundaram & Collins 1999; Ferrante & Elghobashi 2003). In PP-DNS, the grid spacing is chosen to resolve the unladen Kolmogorov length scale η. If the mass loading of the system is large enough, particles carry an additional representation as point sources of momentum in the fluid phase represented by a force applied at the particle centre. The force felt by the fluid is equal in magnitude and opposite in direction to the force felt by a given particle. The point-particle approach has a sound theoretical basis in the limit where the particle diameter d_p is small compared with the Kolmogorov length scale η. However, lack of validation of the point-particle method makes it unclear what happens as the particle size approaches and exceeds the Kolmogorov scale. This is one motivation for the present study.

Because the flow is not resolved at the scale of the particles in the point-particle method (due to small d_p with respect to η) an appropriate particle acceleration model is needed to represent the integrated hydrodynamic stress on each particle. Perhaps the earliest work is owing to Stokes (1850) who found that under the assumption of low Reynolds number, the drag force a particle experiences as it moves in an otherwise quiescent flow is proportional to the particle's velocity. Building on work by Stokes (1850), Boussinesq (1885) and Basset (1888) formulated the particle drag force in unsteady flows. Faxén (1922) developed a generalization of the drag force for non-uniform flows. Corrsin & Lumley (1956) incorporated the known hydrodynamic interactions into a particle equation of motion. Maxey & Riley (1983) and Gatignol (1983) proposed a general particle equation of motion which includes a complete description of forces on a particle. The Maxey–Riley–Gatignol (MRG) equation is valid for a rigid particle moving at low particle Reynolds number, ($Re_p = d_p|\tilde{\boldsymbol{u}}^{(f)} - \boldsymbol{V}|/\nu^{(f)} \ll 1$ with $\tilde{\boldsymbol{u}}^{(f)}$ being the undisturbed fluid velocity at the particle centre, $\boldsymbol{V}$ being the particle velocity and $\nu^{(f)}$ being the fluid-phase kinematic

viscosity), in a Newtonian fluid away from solid boundaries and takes into account viscous (Stokes) drag, Faxén corrections, added mass, fluid acceleration, buoyancy and history forces. Here d_p is the particle diameter, $\tilde{\boldsymbol{u}}^{(f)}$ is the undisturbed fluid velocity at the particle location, $\boldsymbol{V}$ is the particle velocity, and $\nu^{(f)}$ is the kinematic viscosity of the fluid. Extensions of the viscous drag to higher Reynolds numbers via the Schiller–Naumann correlation (Clift, Grace & Weber 1978), and the history term (Lovalenti & Brady 1993) have been developed, as well as extensions to compressible flows (Parmar, Haselbacher & Balachandar 2012).

Although the first-order effect of a particle acceleration model is to ensure accurate prediction of particle trajectories due to hydrodynamic forces, the model's role in modifying fluid turbulence statistics cannot be neglected. Particle acceleration plays a key contribution to the interphase turbulent kinetic energy (TKE) transfer arising from interphase interactions (Tenneti *et al.* 2010; Mehrabadi *et al.* 2015). Tenneti, Mehrabadi & Subramaniam (2016) and Mehrabadi & Subramaniam (2017) have showed that interphase TKE transfer is responsible for the transfer of TKE between the fluid and the solid particles resembling the role of the turbulence production term in the context of single-phase flow (Pope 2000). This term is of great importance in modulation of turbulent flow by a dispersed particle phase. Subramaniam *et al.* (2014) studied decaying isotropic particle-laden turbulent flows and showed that while the fluid kinetic energy prediction from PP-DNS is very close to that of PR-DNS, the interphase TKE transfer and the fluid dissipation were significantly different. It was argued that the deficiency was due to the use of an inappropriate particle acceleration model for their choice of parameters. As we will demonstrate in this paper, the choice of acceleration model plays an important role in accurate prediction of interphase energy transfer, though other factors including model implementation also play important roles. Notwithstanding, Schneiders, Meinke & Schroder (2016) have incorporated inertial effects into point-particle models as a means for comparing with turbulent flow statistics predicted by particle-resolved simulations.

While there has been extensive work on the development of particle acceleration models, these models are necessarily incomplete. Under the most general circumstances, there is no way to express the integrated fluid stress on the surface of a particle solely in terms of a finite number of undisturbed fluid quantities. Still, the value of these equations of motion, despite the fact that their origins rest in simplified problems, is that they may nevertheless provide utility in more complicated flows. Therefore, it is worth assessing the validity of present particle acceleration models to determine their accuracy in predicting turbulence modulation and particle statistics.

Experimental efforts are reliable sources to validate particle acceleration models. However, limited optical access into fluidized beds limits the applicability of experimental investigations to either dilute suspensions (Lee & Durst 1982; Rogers & Eaton 1991; Sato, Hishida & Maeda 1996; Oakley, Loth & Adrian 1997; Kiger & Pan 2000) or pseudo two-dimensional experimental settings (Goldschmidt *et al.* 2003; Bokkers, Annaland & Kuipers 2004). Particle-resolved direct numerical simulation (PR-DNS) has emerged as a powerful tool to study turbulent particle-laden suspensions (Balachandar & Eaton 2010; Tenneti & Subramaniam 2014) and hone point-particle models (Tenneti, Garg & Subramaniam 2011). In PR-DNS, no coupling force is assumed. Rather, the fluid structures are resolved at all scales and the particles move owing to the integrated fluid stress on their boundary. PR-DNS has been used to study the interaction of a single particle with decaying (Bagchi & Balachandar 2003; Burton & Eaton 2005) and stationary (Naso & Prosperetti 2010) isotropic turbulence. PR-DNS has also been employed to study the effect of a collection of

particles on homogeneous isotropic turbulence (Cate *et al.* 2004; Zhang & Prosperetti 2005; Lucci, Ferrante & Elghobashi 2011; Gao, Li & Wang 2013; Wang *et al.* 2014; Chouippe & Uhlmann 2015), particle-laden turbulent channel flow (Uhlmann 2008; Kidanemariam *et al.* 2013) as well as gas–solid flow with upstream turbulence (Xu & Subramaniam 2010). In addition, Homann & Bec (2010) have compared particle acceleration variance of neutrally buoyant particles in forced turbulence using PR-DNS and PP-DNS. In the aforementioned studies, the particle diameter is larger than the Kolmogorov length scale, and particle-to-fluid density ratio is of the order of 1. Recently, Subramaniam *et al.* (2014) and Schneiders *et al.* (2016) have been able to perform PR-DNS of Kolmogorov-size particles to analyse modulation of the turbulent flow.

In the current study, we focus on an assumed form of particle acceleration/drag model commonly used in PP-DNS, and use PR-DNS to validate its capability in representing hydrodynamic acceleration in homogeneous decaying isotropic turbulence. We use PR-DNS in a regime that is believed to be applicable to the PP-DNS approach, while retaining the computational feasibility of the PR-DNS. These considerations leave us with a particle-laden flow with particle diameters being equal to the Kolmogorov length scale ($d_p = \eta$), and the turbulent Reynolds number based on the Taylor microscale being $Re_\lambda = 27$. Note that the former meets the upper limit of the PP-DNS applicability, while the latter is due to the significant computational demand required for PR-DNS of small particles in a turbulent flow.

Now assuming that the drag model has been chosen and validated, the point-particle algorithm requires careful numerical implementation. One implementation challenge is that particles may exist anywhere in space, while fluid variables are updated at grid points. Calculation of the force therefore requires interpolation of fluid properties to the particle location, and, in the case of two- and four-way coupling, projection of the drag force back to the fluid. Efforts by Yeung & Pope (1988) and Balachandar & Maxey (1989) solved the zero and one-way coupled interpolation problem. They found that particle trajectories could be accurately tracked by using a sufficiently high-order interpolation scheme to interpolate the local fluid variables (velocity) to the particle position. For two-way (and four-way) coupled problems, the drag force at the particle position must be projected back to the Eulerian grid. For particles obeying Stokes drag (evaluated using the disturbed fluid velocity), Sundaram & Collins (1996) showed that the total energy equation for the particles and fluid would only be numerically consistent if the weights used for interpolation of fluid quantities to the particle position were the same as the weights used to project information from the particles back to the fluid.

Another challenge in two-way coupled problems is the drag force dependence on undisturbed fluid quantities; for example, Stokes drag depends on the difference between the undisturbed fluid velocity evaluated at the particle position and the particle's velocity. However, in two-way coupled simulations, the fluid velocity field near each particle is contaminated by that particle's own disturbance flow. Some recent efforts to estimate the undisturbed fluid velocity have been proposed (Gualtieri *et al.* 2015; Horwitz & Mani 2016; Ireland & Desjardins 2017). The Gualtieri *et al.* (2015) and Ireland & Desjardins (2017) studies are based on analytical solutions developed for a regularized point force and are exact in the limit of large filter width compared to particle size, while the Horwitz & Mani (2016) study is based on empirical numerical tests and also takes into account the numerical discretization. Each method shows similar accuracy with regard to predicting the settling velocity of an isolated particle under laminar conditions. In this study, we will use the method

presented in Horwitz & Mani (2016) and its extension to higher particle Reynolds numbers (Horwitz & Mani 2018).

Having identified the aforementioned challenges, the motivation of the present study is to explore the question, can a point-particle simulation reproduce the statistics of a particle-resolved simulation of the same non-dimensional problem? To answer this question, we perform simulations of a monodisperse particle configuration in decaying isotropic turbulence. Particles are seeded with the local fluid velocity and the system evolves in time. With the same nominal initial condition, we explore how the statistics of the particle-resolved simulations compare with those obtained from point-particle simulations. Point-particle simulations both accounting and not accounting for the undisturbed fluid velocity in the particle acceleration model are considered. We perform our analysis for two particle Stokes numbers $St_\eta = 1$ and $St_\eta = 100$. The goal is to assess the validity of particle acceleration models used in gas–solid flow simulations. We also highlight the importance of numerical implementation on model predictions. The rest of the paper is organized as follows: In § 2, we present the kinetic energy equation for a homogeneous monodisperse particle-laden suspension and discuss the impact of the acceleration model on modifying the energy exchange process between particles and fluid. In § 3 we present the numerical methodology for the particle-resolved and point-particle approaches. Results obtained using both approaches are directly compared in § 4 and discussed in § 5, while concluding remarks are provided in § 6.

2. Implication of gas–particle drag model on higher-order statistics

In gas–solid suspensions, the two phases are coupled through interphase interactions. In this regard, the drag force plays a fundamental role in interphase momentum transfer, but it also directly contributes to the interphase turbulent kinetic energy transfer which determines the level of gas-phase and solid-phase velocity fluctuations.

The solid-phase kinetic energy can be partitioned into translational and rotational components. The rotational energy transfer occurs through hydrodynamic interactions when particles experience a local velocity gradient at a length scale comparable to the particle diameter, or through collisions between non-spherical or non-smooth particles. The particles in this study are spherical and smooth so that the tangential component of the collision force is neglected. Low particle collision frequency, consistent with low solid-phase volume fraction ($\phi = 0.001$), means that the momentum and energy transfer due to particle collisions is negligible. We may therefore estimate the magnitude of the translational to rotational kinetic energy purely based on hydrodynamics. Particles will be initialized with the local fluid velocity with no rotation. Therefore, the particle translational velocity scales as the root mean square (r.m.s.) fluid velocity u'. The particle size being equal to the initial Kolmogorov scale and manner of seeding together suggest that particles would not be able to develop a rotation rate Ω larger than $O(\tau_\eta^{-1})$, where τ_η is the Kolmogorov time. The respective translational and rotational kinetic energies will scale as $k^{(p)}_{trans} \sim (1/2)m_p u'^2$ and $k^{(p)}_{rot} \sim (1/2)I\tau_\eta^{-2}$, where $I = (2/5)m_p(d_p/2)^2$ is the moment of inertia for a solid sphere. Since the particle size is equal to the initial Kolmogorov scale η_0, using $u_{\eta_0} = \eta_0/\tau_{\eta_0}$ and the initial values for the Kolmogorov and r.m.s. fluid velocity, the ratio of particle rotational to translational kinetic energy may be estimated as $k^{(p)}_{rot}/k^{(p)}_{trans} = (2/5)(d_p/2)^2|\Omega_i\Omega_i|/|v_i v_i| \sim (1/10)(u_{\eta_0})^2/u_0'^2 = O(10^{-2})$. This scaling analysis indicates that the translational kinetic energy of the particles will be dominant, and therefore we neglect the rotational kinetic energy from the remainder of the analysis.

In this study we are interested in examining the implication of particle acceleration and its numerical implementation on the kinetic energy of fluctuating velocities in the fluid phase $k^{(f)}$ and the solid phase $k^{(p)}$ as well as the viscous dissipation $\varepsilon^{(f)}$. Therefore, in this section we briefly review the equations governing the TKE in each phase.

2.1. *Kinetic energy equations*

In the context of multiphase flow, the conservation equations are derived from statistical approaches. One such statistical procedure used in gas–solid flow is the random field (RF) approach (Pai & Subramaniam 2009; Tenneti & Subramaniam 2014; Mehrabadi & Subramaniam 2017). In this approach the transport equations of mass, momentum and energy are multiplied by a phasic indicator function $I^{(\beta)}$ with $\beta \in (f, p)$ which is 1 in phase β and 0 otherwise. Here, (f) and (p) denote the fluid and particle phases, respectively. The equations are then ensemble averaged over all possible realizations in the event space. If the system is statistically homogeneous and ergodic, then ensemble averaging and volume averaging are equivalent. Therefore, the mean value of property Q in phase β is given by

$$\langle Q^{(\beta)} \rangle = \frac{\langle I^{(\beta)} Q \rangle}{\langle I^{(\beta)} \rangle} = \frac{\int I^{(\beta)} Q \, \mathrm{d}V}{\int I^{(\beta)} \, \mathrm{d}V}, \tag{2.1}$$

and subsequently the fluctuating component is defined as $Q'^{(\beta)} = Q - \langle Q^{(\beta)} \rangle$. It is worth mentioning that in the above equation the denominator represents the volume fraction of phase β.

Accordingly, the level of kinetic energy in phase β is defined as $k^{(\beta)} = \langle \boldsymbol{u}'^{(\beta)} \cdot \boldsymbol{u}'^{(\beta)} \rangle / 2$ with the velocity fluctuation being $\boldsymbol{u}'^{(\beta)} = \boldsymbol{u}^{(\beta)} - \langle \boldsymbol{u}^{(\beta)} \rangle$ (in the present study, $\langle \boldsymbol{u}^{(\beta)} \rangle$ is zero). The evolution equations of gas-phase and solid-phase kinetic energy for a homogeneous gas–solid suspension are, respectively, given by (Pai & Subramaniam 2009; Subramaniam *et al.* 2014; Mehrabadi *et al.* 2015)

$$\rho^{(f)}(1-\phi)\frac{\mathrm{d}k^{(f)}}{\mathrm{d}t} = \Pi^{(f)} - \varepsilon^{(f)}, \tag{2.2}$$

$$\rho^{(p)}\phi\frac{\mathrm{d}k^{(p)}}{\mathrm{d}t} = \Pi^{(p)}. \tag{2.3}$$

In the above equations, it is assumed that the rotational energy of particles is negligible compared to the translational kinetic energies. Also, the particles are assumed to be elastic, so that collisions make no net contribution to energy exchanges. In the above equations, $\rho^{(f)}$ and $\rho^{(p)}$ are the gas-phase and solid-phase mass densities, ϕ is the solid-phase volume fraction, and $\varepsilon^{(f)} = 2\mu^{(f)}\langle I^{(f)} \boldsymbol{s}_{ij}\boldsymbol{s}_{ij} \rangle$ ($\boldsymbol{s}$ being the strain-rate tensor) is the viscous dissipation (Subramaniam *et al.* 2014; Mehrabadi *et al.* 2015). In addition, $\Pi^{(f)}$ and $\Pi^{(p)}$ are respectively the fluid-phase and solid-phase interphase TKE transfer terms. It has been shown (Xu & Subramaniam 2007; Mehrabadi *et al.* 2015; Mehrabadi & Subramaniam 2017) that the interphase TKE transfer terms, arising from the velocity fluctuation–drag force covariance, play key roles in transfer of the kinetic energy due to interphase interactions. By definition, these transfer terms have the following forms:

$$\Pi^{(f)} = -\langle \boldsymbol{u}^{(f)} \cdot \boldsymbol{f} \rangle, \tag{2.4}$$

$$\Pi^{(p)} = \langle \boldsymbol{u}^{(p)} \cdot \boldsymbol{f} \rangle, \tag{2.5}$$

where $\boldsymbol{f} = -\boldsymbol{\sigma} \cdot \nabla I^{(p)}$ is the interfacial force per unit volume, and $\boldsymbol{\sigma}$ is the fluid stress tensor. It is worth mentioning that the gradient of the indicator function can be rewritten as $-\boldsymbol{n}^{(p)}\delta(\boldsymbol{x} - \boldsymbol{x}^{(I)})$ (Drew & Passman 1998), where $\boldsymbol{n}^{(p)}$ is the normal vector at each particle surface, and $\delta(\boldsymbol{x} - \boldsymbol{x}^{(I)})$ is a generalized delta function which is non-zero only at the fluid–solid interface. The alternative form of the drag force $\boldsymbol{f} = \boldsymbol{\sigma} \cdot \boldsymbol{n}^{(p)}\delta(\boldsymbol{x} - \boldsymbol{x}^{(I)})$ is particularly useful since the computed drag force (integral of the fluid stress over the particle surface) in PR-DNS is reconcilable with this definition. In addition, it has been shown that this definition in conjunction with the kinematic condition at the interface leads to the conservation of the interphase TKE transfer principle which states that, for the case of zero mean-slip velocity, the interphase transfer terms are equal in magnitude and opposite in sign, i.e. $\Pi^{(f)} + \Pi^{(p)} = 0$ (Xu & Subramaniam 2007; Mehrabadi *et al.* 2015; Mehrabadi & Subramaniam 2017). This implies that the rate of energy lost by one phase owing to interphase interactions at mutual fluid–solid interfaces is equal in magnitude to the rate of energy gained by the other phase. As a result, the mixture kinetic energy $e^{(m)}$ defined as $\rho^{(f)}(1-\phi)k^{(f)} + \rho^{(p)}\phi k^{(p)}$, which is the mass-weighted kinetic energy in the system governed by:

$$\frac{\mathrm{d}e^{(m)}}{\mathrm{d}t} = \Pi^{(f)} + \Pi^{(p)} - \varepsilon^{(f)}, \tag{2.6}$$

simplifies to

$$\frac{\mathrm{d}e^{(m)}}{\mathrm{d}t} = -\varepsilon^{(f)}. \tag{2.7}$$

Therefore, the mixture energy decays monotonically due to the viscous dissipation in the absence of any driving force. This equation is also reconcilable with the PR-DNS formulation in which the drag force on each particle surface is directly recovered. Nevertheless, this conservation principle is violated by PP-DNS (or any other numerical approach) in which a particle drag model is used in place of direct enforcement of no-slip and no-penetration boundary conditions at particle surfaces.

2.2. *Point-particle model kinetic energy equations*

In the PP-DNS implementation, the drag force on particle i, i.e. $\boldsymbol{F}_{i,pp}$ is provided by an assumed drag model. To project this drag force to the Eulerian grid, the following expression is used:

$$\boldsymbol{f}_{pp} = \frac{1}{V_{cell}} \sum_{i=1}^{N_p} \boldsymbol{F}_{i,pp} \mathcal{P}(\delta(\boldsymbol{X}_i - \boldsymbol{x})). \tag{2.8}$$

In the above equation, the subscript pp denotes point-particle quantities. In addition, the operator $\mathcal{P}(\delta(\boldsymbol{X}_i - \boldsymbol{x}))$ is the numerical projection operator that is non-zero on the grid points of the corresponding Eulerian cell with the cell volume V_{cell}. Considering the above definition for the point-particle drag force, the evolution equations for implied fluid-phase and solid-phase velocity fluctuations are (Sundaram & Collins 1999; Subramaniam *et al.* 2014)

$$\rho^{(f)}(1-\phi)\frac{\mathrm{d}k_{pp}^{(f)}}{\mathrm{d}t} = \Pi_{pp}^{(f)} - \varepsilon_{pp}^{(f)}, \tag{2.9}$$

$$\rho^{(p)}\phi\frac{\mathrm{d}k_{pp}^{(p)}}{\mathrm{d}t} = \Pi_{pp}^{(p)}. \tag{2.10}$$

In (2.9), $-\varepsilon_{pp}^{(f)} \equiv (1-\phi)(1/V)\int \mu^{(f)}\boldsymbol{u}^{(f)}\nabla^2\boldsymbol{u}^{(f)}\,\mathrm{d}V$, and the integration is over the whole fluid volume V. Using the modelled drag force in (2.8), the implied interphase TKE transfer terms in the PP-DNS formulation now have the following forms:

$$\Pi_{pp}^{(f)} = (1-\phi)\frac{1}{V}\sum_{i=1}^{N_p}\boldsymbol{u}^{(f)}(\boldsymbol{X}_i)\cdot\boldsymbol{F}_{i,pp}, \tag{2.11}$$

$$\Pi_{pp}^{(p)} = \frac{1}{V}\sum_{i=1}^{N_p}\boldsymbol{V}_i\cdot\boldsymbol{F}_{i,pp}. \tag{2.12}$$

In (2.11) and (2.12), $\boldsymbol{u}^{(f)}(\boldsymbol{X}_i)$ represents the fluid velocity at the ith particle location, and $\boldsymbol{V}_i$ is the particle velocity. The mixture energy for point particles, $e_{pp}^{(m)} = \rho^{(f)}(1-\phi)k_{pp}^{(f)} + \rho^{(p)}\phi k_{pp}^{(p)}$, can then be expressed as:

$$\frac{\mathrm{d}e_{pp}^{(m)}}{\mathrm{d}t} = \Pi_{pp}^{(f)} + \Pi_{pp}^{(p)} - \varepsilon_{pp}^{(f)}. \tag{2.13}$$

The summation of the interphase TKE transfer terms in the above equations reveals that

$$\Pi_{pp}^{(f)} + \Pi_{pp}^{(p)} = \frac{1}{V}\sum_{i=1}^{N_p}(\boldsymbol{V}_i - \boldsymbol{u}^{(f)}(\boldsymbol{X}_i))\cdot\boldsymbol{F}_{i,pp} + O(\phi^2). \tag{2.14}$$

In (2.14), the additional term which is $O(\phi^2)$ (see appendix A) is an error consistent with the neglect of volume fraction in the point-particle equations. The kinematic constraint of zero relative velocity at particle surfaces which is enforced by the PR-DNS method, does not hold for the PP-DNS method, i.e. $\boldsymbol{V}_i - \boldsymbol{u}^{(f)}(\boldsymbol{X}_i) \neq 0$. As a result, the summation of $\Pi_{pp}^{(f)}$ and $\Pi_{pp}^{(p)}$ in (2.14) is non-zero which means that the conservation of interphase TKE transfer principle does not hold. In the PP-DNS formulation, equation (2.14) is interpreted as an additional dissipation near particle surfaces, and is denoted as ε_{pp}^{*} (Sundaram & Collins 1999; Xu & Subramaniam 2007). The additional dissipation can be interpreted as the model-form dissipation arising from the fact that not all of the true fluid dissipation is resolved by the term, $\varepsilon_{pp}^{(f)}$. Therefore, the use of a particle acceleration model for fluid–solid interactions in the PP-DNS approach leads to a different form of the mixture energy equation, that is

$$\frac{\mathrm{d}e^{(m)}}{\mathrm{d}t} = -\varepsilon_{pp}^{*} - \varepsilon_{pp}^{(f)}, \tag{2.15}$$

which is now governed by the under-resolved viscous dissipation $\varepsilon_{pp}^{(f)}$ and a model for the additional dissipation near particle surfaces ε_{pp}^{*}.

The formulations for the TKE equations presented here show that no direct comparison is possible between viscous dissipation obtained from PR-DNS and PP-DNS approaches (cf. equations (2.7) and (2.15)) unless the effect of the additional dissipation near particle surfaces ε_{pp}^{*} is accounted for (Sundaram & Collins 1996, 1999; Subramaniam *et al.* 2014; Horwitz & Mani 2016). In this study it is of interest to investigate the effect of the gas–particle drag force in the PP-DNS approach on the implied statistics of turbulence when compared with those of the PR-DNS. Further details of the point-particle energetics derivation can be found in appendix A.

3. Numerical methods

We perform PR-DNS and PP-DNS of decaying isotropic turbulent particle-laden flow. The simulations are carried out using two codes which facilitate appropriate implementations for PR-DNS and PP-DNS approaches. Details of these approaches are given in this section.

3.1. *Particle-resolved direct numerical simulation*

PR–DNS of freely evolving gas–solid suspensions are performed using the particle-resolved uncontaminated-fluid reconcilable immersed boundary method (PUReIBM) that has been developed to simulate flow past fixed particle assemblies (Garg *et al.* 2011; Tenneti *et al.* 2013; Mehrabadi *et al.* 2015; Sun, Tenneti & Subramaniam 2015; Mehrabadi, Murphy & Subramaniam 2016*a*; Sun *et al.* 2016) and freely evolving suspensions (Tenneti *et al.* 2016; Mehrabadi, Tenneti & Subramaniam 2016*b*). In PUReIBM, the entire physical domain is discretized using a uniform Cartesian grid and the governing equations of fluid flow are solved on all the grid points (including those lying inside the particles). The governing equations that are solved in PUReIBM are the continuity equation

$$\boldsymbol{\nabla}\cdot\boldsymbol{u}=0, \tag{3.1}$$

and the Navier–Stokes equations

$$\rho^{(f)}\frac{\partial \boldsymbol{u}}{\partial t}+\rho^{(f)}\boldsymbol{\nabla}\cdot(\boldsymbol{uu})=-\boldsymbol{\nabla}p+\mu^{(f)}\nabla^2\boldsymbol{u}+\boldsymbol{f}_{IB}, \tag{3.2}$$

where $\boldsymbol{u}$ and p are respectively the instantaneous velocity and pressure fields. The third term on the right-hand side of (3.2) is the immersed boundary (IB) force $\boldsymbol{f}_{IB}$ that accounts for the presence of solid particles by enforcing the no-slip and no-penetration boundary conditions at the surface of the particles. Complete details of the computation of the IB force can be found in the work of Tenneti *et al.* (2011). The surface of the spherical particle is represented by a discrete number of Lagrangian points called boundary points that are parametrized in spherical coordinates. Two additional sets of points, termed as exterior and interior points are generated by projecting the boundary points onto spheres of radii $r+\Delta r$ and $r-\Delta r$ respectively, with Δr chosen to be equal to the grid spacing. In PUReIBM, the IB force is computed only at the interior points so that a desired velocity $\boldsymbol{u}^{(d,k)}$ is obtained at the kth interior point with respect to the nth time step. Following the direct forcing method proposed by Mohd-Yusof (1996) the IB force $\boldsymbol{f}_{IB}^{(k)}$ at the kth interior point is computed as:

$$\boldsymbol{f}_{IB}^{(k)}=\rho^{(f)}\frac{\boldsymbol{u}^{(k,d)}-\boldsymbol{u}^{(k,n)}}{\Delta t}+\rho^{(f)}\boldsymbol{\nabla}\cdot(\boldsymbol{uu})^{(k,n)}+\boldsymbol{\nabla}p^{(k,n)}-\mu^{(f)}\nabla^2\boldsymbol{u}^{(k,n)}. \tag{3.3}$$

The desired velocity $\boldsymbol{u}^{(k,d)}$ depends on the velocity of the particle. For instance, for a fixed particle the desired velocity at the interior point is equal in magnitude but opposite in direction of the fluid velocity at the corresponding exterior point so that the velocity at the boundary point is zero. The IB force computed at all the interior points is distributed among the neighbouring Cartesian grid nodes, but limited only to those grid points in solid particles.

It has been shown by Tenneti *et al.* (2011) that volume-averaged equations in a periodic domain can be reconciled with the ensemble-averaged equations of

statistically homogeneous gas–solid suspensions. Hence the governing equations (3.1) and (3.2) are solved numerically in a cubic domain with periodic boundaries, since the primary goal is to simulate statistically homogeneous suspensions. Similar to DNS of single-phase turbulence, it is simpler to solve for appropriately defined fluctuating variables. The velocity field is decomposed into a spatially uniform mean flow $\langle \boldsymbol{u} \rangle_{\mathcal{V}}(t)$ and a fluctuating velocity field $\boldsymbol{u}'(\boldsymbol{x}, t)$, i.e.

$$\boldsymbol{u}(\boldsymbol{x}, t) = \langle \boldsymbol{u} \rangle_{\mathcal{V}}(t) + \boldsymbol{u}'(\boldsymbol{x}, t), \tag{3.4}$$

where the volumetric mean velocity is obtained by averaging the velocity field over the entire computational domain. Similar decompositions are written for the convective term, the pressure gradient ∇p and IB force $\boldsymbol{f}$. It should be noted that the mean values of the velocity, pressure gradient and immersed boundary forcing are zero in an isotropic turbulent flow. Substituting the above decompositions in (3.1) and (3.2), followed by averaging over the entire computational domain yields the volume-averaged mass and momentum conservation equations (detailed equations are given by Tenneti *et al.* (2011)). Evolution equations for the fluctuating variables are derived by subtracting the volume-averaged equations from their instantaneous counterparts. The resulting equations for the fluctuating variables are solved using a pseudo-spectral method, with the Crank–Nicolson scheme for the viscous terms, and an Adams–Bashforth scheme for the convective terms. A fractional time-stepping method based on the work of Kim & Moin (1985) is used to advance the fluctuating velocity fields in time.

In freely evolving gas–solid suspensions, the particles move under the influence of hydrodynamic and collisional forces. In PUReIBM, the particles are represented in a Lagrangian frame of reference. The position and translational velocity of the ith particle at time t are denoted by $\boldsymbol{X}_i(t)$ and $\boldsymbol{V}_i(t)$ respectively, and they evolve in time as:

$$\frac{\mathrm{d}\boldsymbol{X}_i(t)}{\mathrm{d}t} = \boldsymbol{V}_i(t), \tag{3.5}$$

$$m_p \frac{\mathrm{d}\boldsymbol{V}_i(t)}{\mathrm{d}t} = \boldsymbol{F}_i(t) + \sum_{\substack{j=1 \\ j \neq i}}^{N_p} C_{ij}(t), \tag{3.6}$$

where $m_p = \rho_p \pi d_p^3/6$ is the particle mass, and N_p is the total number of particles used in the simulation. Here $\boldsymbol{F}_i$ is the hydrodynamic force calculated from the velocity and pressure fields at the particle surface. Also C_{ij} is the contact force on the ith particle as a result of collision with the jth particle, and is treated using a soft-sphere model originally proposed by Cundall & Strack (1979). For the present study, the collisions are modelled as elastic. Nevertheless, since the suspension is very dilute in the cases studied here, particle collisions are infrequent. Some more discussion on collision frequency and the effect of collisions on point-particle results is presented in appendix B.

3.2. *Point-particle direct numerical simulation*

The point-particle algorithm is based on the code originally developed by Pouransari, Mortazavi & Mani (2015). The fluid-phase governing equations are the Navier–Stokes equations, (equations (3.1) and (3.2)) but written in conservative form. However, the

immersed boundary force $\boldsymbol{f}_{IB}$ in (3.2) is replaced by the negative of the gas–particle drag evaluated on the Eulerian grid by (2.8), that is

$$-\boldsymbol{f}_{IB} \equiv \boldsymbol{f}_{pp} = \frac{1}{V_{cell}} \sum_{i=1}^{N_p} \boldsymbol{F}_{i,pp} \mathcal{P}(\delta(\boldsymbol{X}_i - \boldsymbol{x})). \tag{3.7}$$

In addition, the particles are tracked in a Lagrangian frame using the same Newtonian laws of motion given in (3.5) and (3.6). The Navier–Stokes equations are solved on a staggered grid using second-order finite differences. The resulting Poisson equation for pressure is solved directly using the fast Fourier transform. Time advancement of both fluid and particle equations is accomplished by explicit fourth-order Runge–Kutta.

To complete the point-particle algorithm, it is necessary to specify the projection operator $\mathcal{P}(\cdot)$, and drag force $\boldsymbol{F}_{i,pp}$. The particles explored in this study will have a size equal to the initial Kolmogorov scale of the fluid, that is $d_p/\eta_0 = 1$. From a scaling perspective, this particle size ratio is borderline in terms of the need to model unsteady effects in the particle equation of motion (Ling, Parmar & Balachandar 2013). As we will show, some of these unsteady effects can be alleviated by seeding the particles with the local fluid velocity rather than at rest, as was done in Subramaniam *et al.* (2014). Faxén corrections are ignored for two reasons. Faxén corrections are important when particles are large enough to see the curvature in the underlying fluid velocity field. Their importance can be shown to scale with the ratio of the particle size to Taylor microscale $(d_p/\lambda)^2$ (Calzavarini *et al.* 2009), which is much smaller than unity for the present problem. However, it is also important to assess whether the curvature induced by the disturbance fields of neighbour particles will be important. Since the volume fraction in this study is relatively low (10^{-3}), the contribution to the Faxén correction owing to disturbance flows created by neighbour particles is small, which provides an additional reason to neglect Faxén corrections. Collisions are also neglected in the point-particle simulation owing to diluteness. In this study we only consider steady drag (Stokes, and Reynolds corrected) and neglect history, added mass, and fluid acceleration forces, to assess whether the simplest version of a point-particle method can find some agreement with a particle-resolved simulation, in the limit where the point-particle method is believed to be valid $d_p/\eta \leqslant 1$. Our goal with this study is validation of the point-particle method, so we were not *a priori* resigned to only use steady drag. Rather we sought to add levels of complexity until statistics from the two approaches agreed within acceptable tolerance. What we will show in the results section, is that an appropriate numerical implementation of steady drag was found to yield good agreement between the two methods, for this particular non-dimensional problem. It is not a universal statement that the drag forces we consider here, and their numerical implementation, will be sufficient for validation problems in other regimes. In this study we consider Stokes (linear) drag, and Schiller–Naumann (nonlinear). Their formulas are:

$$\boldsymbol{F}_i^{St} = 3\pi\mu^{(f)} d_p (\tilde{\boldsymbol{u}}_i^{(f)} - \boldsymbol{V}_i), \tag{3.8}$$

$$\boldsymbol{F}_i^{SN} = 3\pi\mu^{(f)} d_p (\tilde{\boldsymbol{u}}_i^{(f)} - \boldsymbol{V}_i)\,(1 + 0.15 \times Re_p{}^{0.687}), \tag{3.9}$$

with the particle Reynolds number being defined as

$$Re_p = \frac{d_p \rho^{(f)} |\tilde{\boldsymbol{u}}_i^{(f)} - \boldsymbol{V}_i|}{\mu^{(f)}}. \tag{3.10}$$

Note that in the above formulation, $\tilde{\boldsymbol{u}}_i^{(f)}$ is the undisturbed fluid velocity at the ith particle location, the importance of which is discussed in the following section.

3.3. *Consistent numerical implementation of the interphase momentum transfer*

The drag formulas in (3.8) and (3.9) depend on the difference between the undisturbed fluid velocity $\tilde{\boldsymbol{u}}_i^{(f)}$ evaluated at the particle location, and the particle's velocity. The undisturbed fluid velocity is the fluid velocity the particle would see in the absence of that particle. This means the undisturbed fluid velocity evaluated at particle j contains a contribution owing to the summation of velocity disturbances created by all other particles $i \neq j$, but not the disturbance created by particle j. This is a modelling problem because the undisturbed fluid velocity is not readily accessible in the simulation. Usually the fluid velocity interpolated from the surrounding fluid grid points to the particle location is assumed to be approximately equal to the undisturbed fluid velocity. However, when the particle size relative to the grid spacing $\Lambda = d_p/\mathrm{d}x$ is significant, then the fluid velocity interpolated to particle j will contain a significant contribution owing to the disturbance velocity field created by particle j. In other words, if this issue is left untreated, this particle will see its own disturbance field, and the drag force which will be used to update its position (and couple momentum and energy to the fluid) will be incorrectly calculated.

This observation was recognized by Horwitz & Mani (2016) who developed a procedure to estimate the undisturbed fluid velocity given a measured disturbed fluid velocity at the location of the particle. The idea is that the undisturbed fluid velocity as used in the above drag formulas for the jth particle should not include the disturbance created by that particle, but may contain the disturbance information from the other particles. The procedure attempts to remove the self-disturbance portion from the measured disturbed fluid velocity which thereby provides an estimate for the undisturbed fluid velocity seen by that particle. The estimation procedure from that work is:

$$\tilde{\boldsymbol{u}}_p^{(f)} = \boldsymbol{u}_p^{(f)} + C_p\,\mathrm{d}x^2\nabla^2\boldsymbol{u}_p^{(f)}. \tag{3.11}$$

The subscript p in (3.11) denotes quantities evaluated at the location of the particle. Here, C_p is an $O(1)$ correction coefficient reported by Horwitz & Mani (2016) and $\nabla^2\boldsymbol{u}_p^{(f)}$ is the Laplacian of the fluid velocity interpolated to the particle position. Essentially, this correction estimates the undisturbed fluid velocity by adding to the measured fluid velocity at the location of the particle, $\boldsymbol{u}_p^{(f)}$, an estimate for the disturbance created by the particle. The estimate is the Laplacian term. Such a correction is expected to work well provided that the curvature introduced into the fluid velocity field by the particle velocity disturbance is large compared with the underlying curvature already present in the flow. The Laplacian can be decomposed as

$$\nabla^2\boldsymbol{u}_p^{(f)} \approx \nabla^2\boldsymbol{u}_p^{P} + \nabla^2\boldsymbol{u}_p^{F}, \tag{3.12}$$

where $\nabla^2\boldsymbol{u}_p^{P}$ is the curvature in the fluid velocity created by the particle velocity disturbance and $\nabla^2\boldsymbol{u}_p^{F}$ is the underlying curvature in the fluid velocity field in the absence of the disturbance flow. Horwitz & Mani (2016) have shown that the disturbance velocity scales as the characteristic fluid velocity and scales with the particle size relative to the grid Λ, so that $|C_p\,\mathrm{d}x^2\nabla^2\boldsymbol{u}_p^{P}| \approx \Lambda u'$, where u' here is the r.m.s. velocity of the turbulence. The ensemble average magnitude of the curvature in the fluid velocity field, in the absence of the particle may be estimated as: $|\nabla^2\boldsymbol{u}_p^{F}| \sim u'/\lambda^2$, where λ is the Taylor microscale. Therefore, we estimate the ratio of the inherent curvature in the flow to that produced by a point particle as:

$$|C_p\,\mathrm{d}x^2\nabla^2\boldsymbol{u}_p^{F}|/|C_p\,\mathrm{d}x^2\nabla^2\boldsymbol{u}_p^{P}| \sim \frac{C_p\,\mathrm{d}x^2u'/\lambda^2}{\Lambda u'} \sim \frac{d_p^2}{\lambda^2} \ll 1. \tag{3.13}$$

In (3.13) we have made use of the fact that $C_p = O(1)$, and for the present study $\Lambda = 1$. The particle size being equal to the initial Kolmogorov scale ($d_p = \eta_0$) means that the ratio in (3.13) is much less than unity ($d_p^2/\lambda_0^2 \approx 10^{-2}$ for the present cases). In other words, the curvature created by the particles owing to their disturbance fields will be much larger than the inherent curvature in the fluid velocity field. An attempt to estimate the undisturbed fluid velocity using a curvature-based procedure is therefore non-dimensionally justified for this problem. Though we have used scaling analyses above to justify the employed correction procedure for the undisturbed fluid velocity (Horwitz & Mani 2016), we have tested the sensitivity of this scheme in a variety of laminar (Horwitz & Mani 2016, 2018), and turbulent environments (Horwitz & Mani 2015, 2018), and have found the results to be fairly insensitive to non-dimensional particle size or Stokes number. Though not specifically tested in the context of finite Reynolds number corrections to steady drag, we expect the procedures developed by Gualtieri *et al.* (2015) and Ireland & Desjardins (2017) based on analytical solutions would also be applicable in the present configuration since the near field of the regularized point-force solution should vary slowly with Reynolds number (Batchelor 1967). Nevertheless the analytical-based methods developed by Gualtieri *et al.* (2015) and Ireland & Desjardins (2017) rely on sufficiently large filter widths to remove errors associated with discretization of the Gaussian kernel, while the procedure developed in Horwitz & Mani (2016) was developed specifically taking into account the effect of discretization.

The procedure outlined above is formally accurate in the limit of small volume fraction and Reynolds number, and high Stokes number. It was found that the above formula (3.11), with no modifications works well for order-unity Reynolds number in the Schiller–Naumann equation (Horwitz & Mani 2018), the error being of the same order as that which is present in the Schiller–Naumann correlation. In addition, this correction scheme was found to perform reasonably well over a range of Stokes numbers covering the range explored in this study. Therefore, the previous studies demonstrated this correction procedure is verifiable. For simple model problems, our previous work (Horwitz & Mani 2016) suggests that particles will follow the correct trajectories and dissipate the correct rate of mechanical energy implied by those force models. In the next section we explore the validation question: can a verifiable numerical implementation of a drag model for point particles, which is valid for the non-dimensional parameters encountered in the present problem, reproduce the particle and fluid statistics implied by the PR-DNS?

Lastly, to complete the point-particle algorithm, it is necessary to specify the projection operator. The correction scheme developed by Horwitz & Mani (2016) to estimate the undisturbed fluid velocity is consistent with projecting the calculated drag force to the Eulerian grid using trilinear weights. For comparison, we will also perform the point-particle simulations assuming the disturbed fluid velocity is equal to the undisturbed fluid velocity (no correction). For these simulations, we will use trilinear weights both for interpolation of the fluid velocity to the particle location and for projection of the drag force back to the fluid grid. Trilinear interpolation/projection is chosen because it was found to be more accurate for two-way coupled problems than higher-order interpolation (Horwitz & Mani 2016; Horwitz *et al.* 2016).

Before presenting the results, it is worth comparing the implied point-particle dissipation term with the form presented in Sundaram & Collins (1996). As noted by Sundaram & Collins (1996), when Stokes drag (3.8) is assumed for the point-force

model, the sum of the inter-phase energy exchange takes a quadratic form *viz*:

$$\Pi_{pp}^{(f)} + \Pi_{pp}^{(p)} = \rho^{(p)}\phi \left\{ \frac{(\boldsymbol{V} - \boldsymbol{u}_p^{(f)}) \cdot (\tilde{\boldsymbol{u}}_p^{(f)} - \boldsymbol{V})}{\tau_p} \right\}_{N_p}. \tag{3.14}$$

In (3.14), $\{\cdot\}_{N_p}$ denotes an average over all particles. The first slip velocity appearing in (3.14), $(\boldsymbol{V} - \boldsymbol{u}_p^{(f)})$, accounts for the difference between the particle and fluid velocity at the location of the particle while the second slip velocity, $(\tilde{\boldsymbol{u}}_p^{(f)} - \boldsymbol{V})$, involves the undisturbed fluid velocity arising due to the assumption of the Stokes drag model. Note that in the limit where the particle size to grid spacing is much smaller than unity $\Lambda \ll 1$, then the undisturbed fluid velocity $\tilde{\boldsymbol{u}}_p^{(f)}$ evaluated at the particle location is approximately equal to the disturbed fluid velocity $\boldsymbol{u}_p^{(f)}$ which would be found by interpolating to the particle location from the surrounding grid points. In this limit, equation (3.14) is a quadratic form in the continuous sense, but the discrete version of this source term will only be numerically consistent if the operator used for interpolating the gas velocity to the particle has the same weights as those used to project the resulting force back to the fluid grid (Sundaram & Collins 1996). Since this observation, symmetric interpolation–projection has become common practice in the literature. However, if the undisturbed fluid velocity is taken into account, as has been argued elsewhere (Horwitz & Mani 2016, 2018; Horwitz *et al.* 2016), the symmetry in the quadratic form disappears, so that there is no longer a reason to assume the same weights for interpolation as projection. Rather, in the authors' opinion, it is best to compute the assumed force model as accurately as possible (which requires a good estimate of the undisturbed fluid velocity), and to then explore the consequences of that procedure. In other words, how good is the agreement between the point-particle statistics where a drag model is assumed (but computed accurately), and a particle-resolved simulation, where no force model is assumed? This is the question we explore in the next section. We conclude this section by noting that the additional particle dissipation term for an arbitrary force (acceleration) model will take the form:

$$\Pi_{pp}^{(f)} + \Pi_{pp}^{(p)} = \rho^{(p)}\phi\{(\boldsymbol{V} - \boldsymbol{u}_p^{(f)}) \cdot \boldsymbol{A}_{model}\}_{N_p}. \tag{3.15}$$

4. Simulation set-up and results

In this section, we directly compare results obtained from particle-resolved and point-particle simulation of decaying isotropic turbulence. In the following we justify our choice of decaying isotropic turbulence as the canonical flow configuration, rather than statistically stationary turbulent flow or homogeneously sheared particle-laden flow. It is non-trivial to perform PR-DNS of a homogeneous turbulent particle-laden flow where there is sustained inherent turbulence without artificially forcing the flow. In particle-laden flows with finite computational domain sizes such artificial forcing can contaminate the natural dynamics of the system. While in single-phase turbulence one can force at the large scales and simulate the natural dynamics of the energy cascade, current computational limitations do not permit the dynamic range needed to access this range of scales using PR-DNS. Furthermore, inertial particles dynamically interact with fluid eddies of a much larger scale and it is well established that the presence of inertial particles modifies the fluid velocity spectra at large scales. In contrast to unladen homogeneous shear flow where the fluid kinetic energy increases

exponentially (Pope 2000), it may be possible to attain a statistically stationary state with particles for certain values of particle Stokes number and mass loading. However, it is not known at present how to systematically choose these parameters to attain a stationary flow. In addition, the notion of turbulence modulation becomes difficult to interpret when the unladen flow has unbounded energy in time. Therefore, in this study, we focus on the influence of particle acceleration models on phasic kinetic energies and viscous dissipation in the canonical setting of decaying isotropic turbulence.

4.1. *Grid resolution*

Following the recipe of Pope (2000), the grid resolution requirement for PR-DNS can be expressed as

$$N^3 = \left(\frac{\mathcal{L}}{\Delta x}\right)^3 = \left(\frac{\mathcal{L}}{L_{11}}\frac{L_{11}}{L}\frac{L}{\eta}\frac{\eta}{d_p}\frac{d_p}{\Delta x}\right)^3, \tag{4.1}$$

where $\mathcal{L}$ is the domain size, and Δx is grid spacing. In addition, L_{11} and L are, respectively, the turbulent integral and large-eddy length scales (Xu & Subramaniam (2010) reported a similar expression for the grid resolution requirement). Assuming that the length scale ratios L_{11}/L and $\mathcal{L}/L_{11}$ are constant, equation (4.1) can be simplified by exploiting the turbulence scaling expressions $L/\eta = Re_L^{3/4}$ and $Re_\lambda = \sqrt{20 Re_L/3}$ (Pope 2000), that is

$$N^3 \sim Re_\lambda^{9/2}\left(\frac{\eta}{d_p}\right)^3\left(\frac{d_p}{\Delta x}\right)^3. \tag{4.2}$$

The above expression reveals that unlike single-phase turbulence, the grid resolution requirement is strongly affected by the particle size and particle grid resolution. The computational cost increases as d_p/η decreases. In addition, the overall grid resolution is proportional to the cube of the grid spacing across each particle $d_p/\Delta x$. The immense computational demand imposed by the grid resolution requirement limits applicability of the PR-DNS of Kolmogorov-size particles to low-to-moderate Taylor microscale Reynolds numbers. Therefore, in the present study we choose $Re_\lambda \approx 27$, $d_p/\eta = 1$ and $d_p/\Delta x = 12$ for the PR-DNS. Based on these parameters, we estimated the size of the domain to be $\mathcal{L}/d_p = 96$ which leads to $N^3 = 1152^3$ grid points for the PR-DNS. For the PP-DNS, the same parameters are considered, except that the grid spacing is $\Delta x = \eta$ which gives rise to $N^3 = 96^3$ grid points. It is worth mentioning that $\kappa_{max}\eta_0$ (κ_{max} being the highest wavenumber in the domain) for PR-DNS and PP-DNS are, respectively, 37.7 and 3.14. One last note concerns the PR-DNS grid resolution per particle diameter $d_p/\Delta x = 12$, which has been verified to be adequate as shown in appendix C. We also find this grid resolution to be consistent with similar particle-resolved studies (Schneiders *et al.* 2016; Ozel *et al.* 2017).

4.2. *Flow initialization*

Owing to resolution requirements for the particle-resolved simulations, the initial Reynolds number is relatively low, $Re_\lambda \approx 27$. The initial condition for each simulation is a divergence-free random field based on the method of (Rogallo 1981) whose

energy spectrum obeys Pope's model spectrum (Pope 2000). The energy spectrum function has the following form:

$$E(\kappa) = C\varepsilon^{2/3}\kappa^{-5/3} f_L(\kappa L) f_\eta(\kappa\eta), \tag{4.3}$$

where C is a model constant, κ is the wavenumber, ε is the dissipation and L and η are large eddy and Kolmogorov length scales, respectively. The functions f_L and f_η determine the shape of energy-containing and dissipative range of the energy spectrum and have the form

$$\left.\begin{aligned} f_L(\kappa L) &= \left(\frac{\kappa L}{[(\kappa L)^2 + c_L]^{1/2}}\right)^{5/3+p_0} \\ f_\eta(\kappa\eta) &= \exp\{-\beta\{[(\kappa\eta)^4 + c_\eta^4]^{1/4} - c_\eta\}\}. \end{aligned}\right\} \tag{4.4}$$

The model constants p_0 and β are the same as those suggested by Pope (2000), while c_L and c_η are determined by the multi-variable Newton–Raphson method such that the energy and dissipation rate from the spectrum matches those required for the chosen Re_λ with $d_p = \eta_0$. The different resolutions and grid configurations (collocated for the particle-resolved and staggered for the point-particle algorithms) means the respective simulations are using different initial conditions, which implies each initial condition should be interpreted as different realizations of the same turbulence. When the parameters in the model spectrum were chosen to match integral length scales for the two initial conditions, both codes resulted in nearly identical evolution of fluid kinetic energy and dissipation rate in unladen simulations. Based on the aforementioned observations, we do not believe there is a sensitivity in the initial conditions that can account for any differences in the results of the particle-laden simulations. The particles are seeded randomly with uniform probability in the box with the initial particle velocity taken as the local fluid velocity at the particle location. The system is then allowed to evolve via fluid and particle equations. Since the sample paths taken by each particle will be different between the two simulation methodologies, the PR-DNS and PP-DNS studies will be said to be statistically equivalent in a weak sense if moments of the particle and fluid distributions can be matched between the two simulation approaches. The number of particles tracked limits the sampling error. While the initial condition does not correspond to a physical turbulent field, the skewness of the longitudinal velocity derivative reaches a physical value of -0.5 within $O(0.1)$ eddy turnover times so that all salient features in the decay are physical.

In this study, we examine particles whose diameter is equal to the initial Kolmogorov scale, $d_p/\eta_0 = 1$. We also examine two Stokes numbers $St_0 = 1$ and $St_0 = 100$ where the particle Stokes number is defined as $St_0 = (1/18)(\rho^{(p)}/\rho^{(f)})(d_p/\eta_0)^2$. These Stokes numbers are defined based on the initial Kolmogorov time scale. The particle size is held constant between the simulations, so that the increase in Stokes number is accomplished by increasing the particle to fluid density ratio from 18 to 1800 between the two simulation cases. The volume fraction is kept small ($\phi = 0.001$) to ensure particle–particle interactions are a second-order effect. With $\mathcal{L}/d_p = 96$ and $\phi = 0.001$, the total number of particles in the domain is:

$$N_p = \phi\frac{6}{\pi}\left\langle\frac{\mathcal{L}}{d_p}\right\rangle^3 = 1689. \tag{4.5}$$

In addition, the two simulation cases correspond to two mass loading ratios, $\Phi_m = (\rho^{(p)}/\rho^{(f)})\phi = 0.018$ and 1.8.

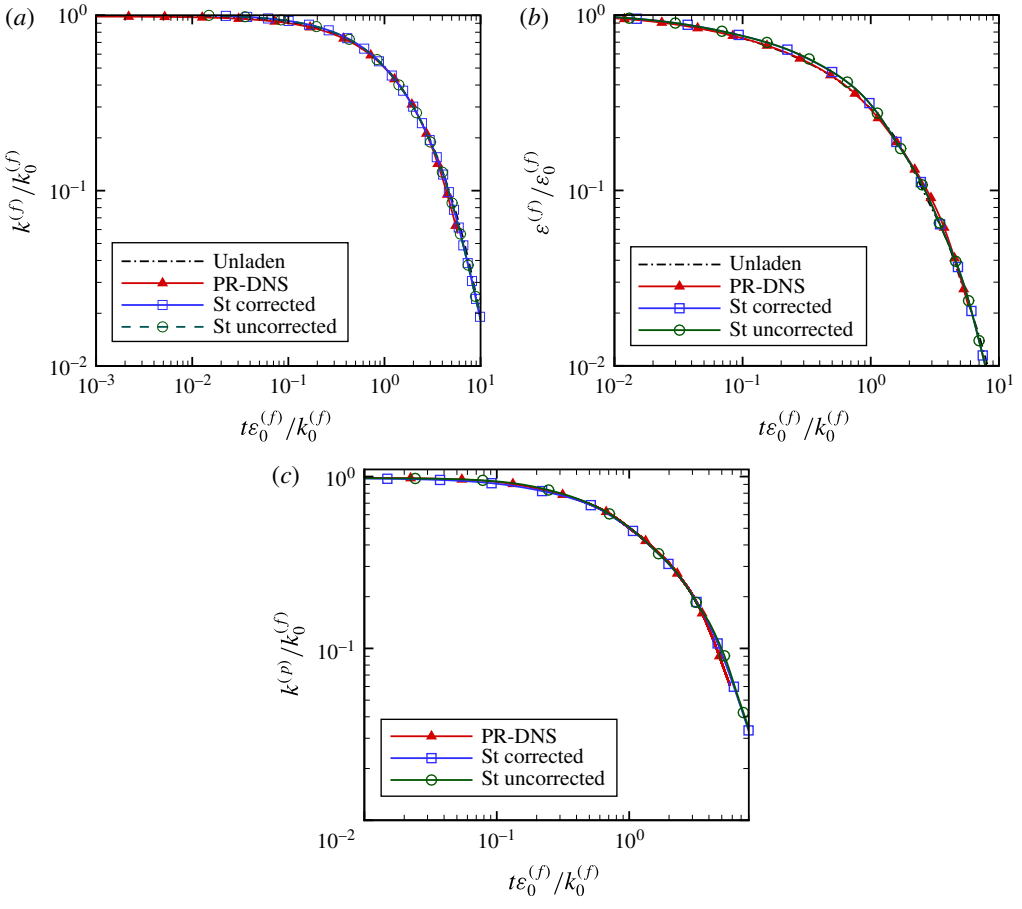

FIGURE 1. (Colour online) Comparison of (*a*) fluid kinetic energy, (*b*) fluid dissipation rate and (*c*) particle kinetic energy versus time from the particle-resolved simulation with different point-particle models for the case $St_0 = 1$. The fluid dissipation rate for the particle-resolved simulation, the right-hand side of (2.7), is compared against the sum of all terms on the right-hand side of (2.13).

4.3. *Fluid and particle statistics for* $St_0 = 1$

The evolution of the fluid energy, dissipation rate, and particle kinetic energy are shown in figure 1. Two point-particle models have been employed; in each, the particles are assumed to obey Stokes drag, however, one of the models accounts for the undisturbed fluid velocity (St corrected) and the other does not (St uncorrected). In comparing statistics, it is clear that both point-particle models are in excellent agreement with the particle-resolved simulation. The agreement between the point-particle simulations and the particle-resolved simulation with regard to fluid energy and dissipation rate is not surprising given the low mass loading. This means the particle–fluid system is effectively one-way coupled. More surprising however is the agreement in particle kinetic energy predicted by the point-particle models compared with the particle-resolved simulation. In the present study, since the particles are initialized with the local fluid velocity, and because the Stokes number is relatively small, the particles never acquire a significant enough slip velocity for

finite Reynolds number corrections to steady drag to become important (as shall be contrasted with the results presented in the next section). This observation also explains why not accounting for the undisturbed fluid velocity has little effect on prediction of particle kinetic energy; at this Stokes number, particles act as tracers to large eddies which dominate contributions to the kinetic energy. This observation also helps explain some of the results presented in Subramaniam *et al.* (2014) which compared point particles and resolved particles at $St_0 = 1$ in decaying isotropic turbulence where the particles were initialized at rest. Though fluid energy was matched well between the two simulation methodologies, the fluid dissipation rate and particle kinetic energies showed disagreement. Therefore it seems the manner in which particles are initialized plays an important role in determining whether inertial and/or unsteady contributions to drag will be significant, as well as how these forces ultimately correlate to other particle and fluid statistics.

4.4. *Fluid and particle statistics for* $St_0 = 100$

In this section we explore a set-up which is of greater relevance to practical gas–solid flows. Owing to the low mass loading for the $St_0 = 1$ case, there was small particle–turbulence interaction. In contrast, the present case exhibits significant coupling between the dispersed and carrier phases. Here the mass loading is increased by a factor of 100 to $\Phi_m = 1.8$. This is accomplished by keeping the particle diameter to initial Kolmogorov scale fixed at $d_p/\eta_0 = 1$ and increasing the density ratio to $\rho^{(p)}/\rho^{(f)} = 1800$.

Fluid kinetic energy and dissipation rate for the present case are shown in figure 2. In contrast with the previous case ($St_0 = 1$), it is clear in the present case ($St_0 = 100$) that significant turbulence modulation is experienced in the fluid. Here we are showing a comparison of the particle-resolved simulation with four point-particle simulations; two of the point-particle simulations employ Stokes drag, with the difference being that one accounts for the undisturbed fluid velocity (St corrected) while the other does not (St uncorrected). The two other point-particle simulations employ the Schiller–Naumann Reynolds-number corrected steady drag formula; the difference in the Schiller–Naumann implementations is again that in one procedure the undisturbed fluid velocity is estimated (SN corrected), while in the other the disturbed fluid velocity is used (SN uncorrected).

In the present case a clear difference is observed among the different point-particle simulations compared with the particle-resolved simulation. The point-particle simulations where the particles obey the Schiller–Naumann drag correlation whose slip velocity is calculated as the difference between the undisturbed fluid velocity and the particle velocity, show excellent agreement in both the fluid kinetic energy and dissipation rate compared with the particle-resolved simulation. The greatest discrepancy is seen between the particle-resolved simulation and the St uncorrected simulation. Interestingly, the St corrected implementation shows better agreement with the particle-resolved simulation than the SN uncorrected scheme. This is an interesting observation which indicates that, at least for the present set-up, it is more important to get the undisturbed fluid velocity right than to use the most applicable drag correlation. Notwithstanding, accounting for both the undisturbed fluid velocity in the drag correlation, and finite Reynolds number corrections to the drag formulation are necessary for agreement between the particle-resolved and point-particle simulation. Despite the particle size being borderline for the importance of unsteady effects (Ling *et al.* 2013; Olivieri *et al.* 2014; Daitche 2015), good agreement between the

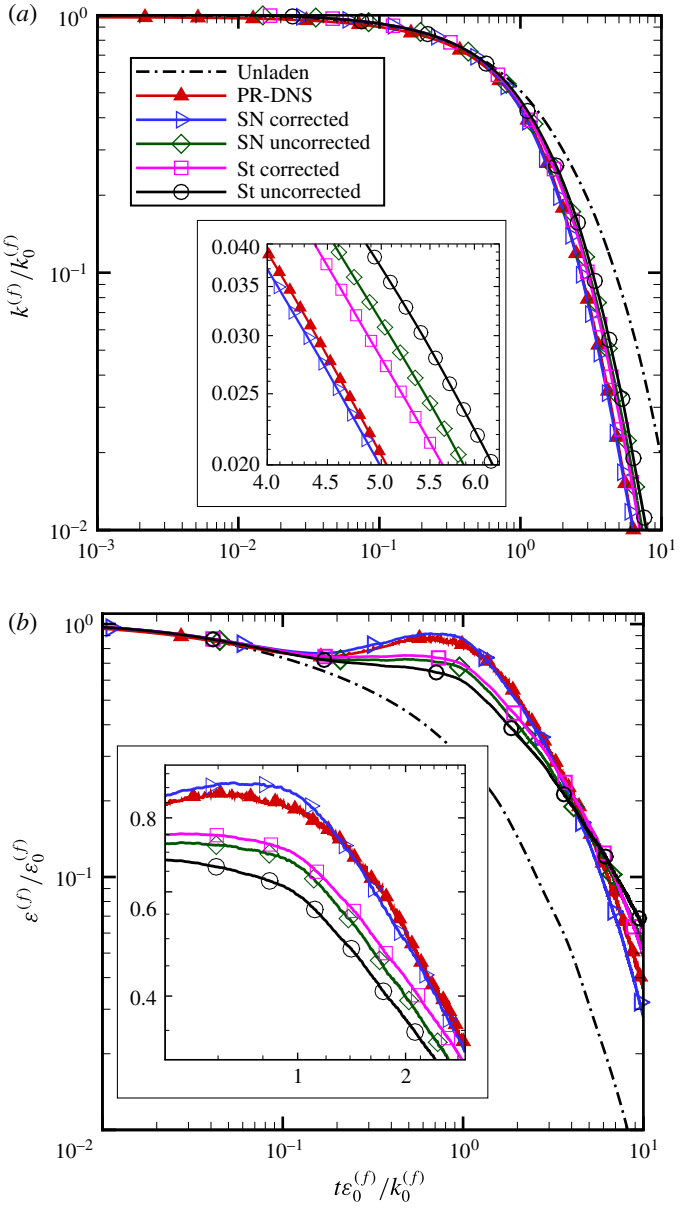

FIGURE 2. (Colour online) Comparison of (*a*) fluid kinetic energy and (*b*) fluid dissipation rate versus time from particle-resolved simulation with different point-particle models for the case $St_0 = 100$. The fluid dissipation rate for the particle-resolved simulation, the right-hand side of (2.7), is compared against the sum of all terms on the right-hand side of (2.13). Both figures share the same line legends.

point-particle and particle-resolved simulation is found without explicitly accounting for these effects in the point-particle model. We have also conducted tests of particles moving in simple flows using the analytical solutions provided by Coimbra & Rangel (1998) and those results provide justification that the history term can be neglected for the present case.

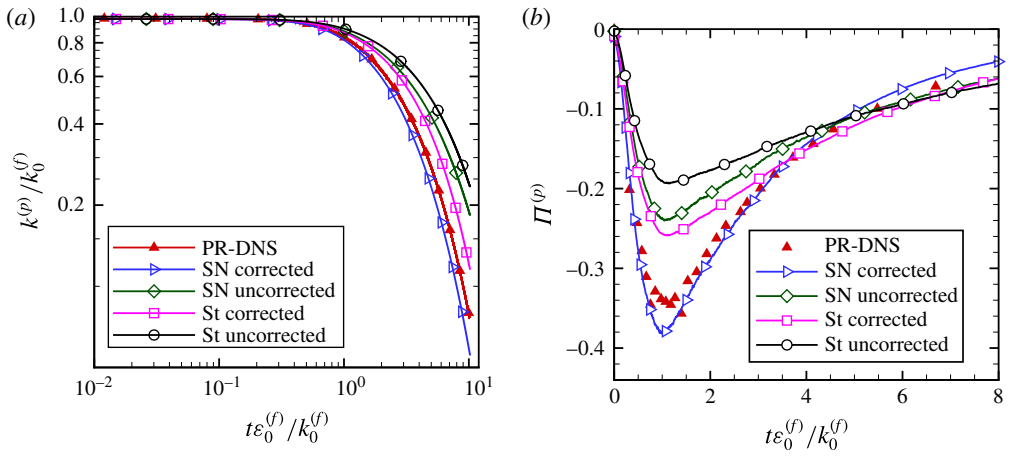

FIGURE 3. (Colour online) Comparison of particle-resolved simulation against different point-particle models for the case $St_0 = 100$, (*a*) particle kinetic energy, and (*b*) solid-phase interphase kinetic energy transfer versus time.

$t\varepsilon_0^{(f)}/k_0^{(f)}$	0.54	2.70	4.87
PR-DNS	0.9303 ± 0.0339	0.5172 ± 0.0179	0.2855 ± 0.0099
SN corrected	0.9267 ± 0.0335	0.4732 ± 0.0162	0.2423 ± 0.0079
St corrected	0.9437 ± 0.0344	0.6071 ± 0.0218	0.3761 ± 0.0136
SN uncorrected	0.9488 ± 0.0345	0.6428 ± 0.0219	0.4363 ± 0.0142
St uncorrected	0.9546 ± 0.0348	0.6987 ± 0.0246	0.5045 ± 0.0174

TABLE 1. The 95 % confidence intervals on particle kinetic energy at different times for PR-DNS and PP-DNS cases for $St_0 = 100$. These quantities are normalized by the initial fluid kinetic energy $k_0^{(f)}$.

The behaviour of the point-particle curves observed in figure 2 is also observed in the particle kinetic energy and dissipation rate shown in figure 3. The SN corrected point-particle scheme shows excellent agreement for particle kinetic energy compared with the PR-DNS. As before, St corrected is more accurate than SN uncorrected, and St uncorrected is the least accurate. To ensure the computation of $k^{(p)}$ is not subject to substantial statistical variability due to the finite number of particles ($N_p = 1689$) in the computational domain, we have calculated 95 % confidence intervals on particle kinetic energy at different times for PR-DNS and PP-DNS, as shown in table 1. The low statistical variability for both PR-DNS and PP-DNS results provide confidence that the observed differences in $k^{(p)}$, especially at later times when particles have lost memory of their initial conditions, are primarily owing to the model form of drag and its implementation rather than sampling error.

Given that the particle kinetic energy in the particle-resolved simulation and SN corrected simulation are in good agreement, the source term that creates particle kinetic energy, namely the covariance of particle velocity and acceleration (see equations (2.5) and (2.12)), must also be in good agreement. Indeed, figure 3(*b*) reveals excellent agreement between the SN corrected scheme and the particle-resolved simulation. The SN corrected scheme predicts a slightly higher peak in particle

$t\varepsilon_0^{(f)}/k_0^{(f)}$	0.54		2.70		4.87	
	$\lvert\boldsymbol{a}_p\rvert$	$\sigma_{\lvert\boldsymbol{a}_p\rvert}$	$\lvert\boldsymbol{a}_p\rvert$	$\sigma_{\lvert\boldsymbol{a}_p\rvert}$	$\lvert\boldsymbol{a}_p\rvert$	$\sigma_{\lvert\boldsymbol{a}_p\rvert}$
PR-DNS	0.052	0.031	0.044	0.021	0.030	0.013
SN corrected	0.058	0.038	0.049	0.024	0.031	0.014
St corrected	0.039	0.021	0.039	0.016	0.029	0.012
SN uncorrected	0.034	0.023	0.033	0.017	0.024	0.011
St uncorrected	0.028	0.016	0.028	0.013	0.022	0.010

TABLE 2. Mean ($\lvert\boldsymbol{a}_p\rvert$) and standard variation ($\sigma_{\lvert\boldsymbol{a}_p\rvert}$) of the particle acceleration magnitude at different times for the PR-DNS compared with the PP-DNS cases for $St_0 = 100$. These quantities are normalized by the initial Kolmogorov velocity scale u_η and time scale τ_η.

velocity–acceleration covariance. This is consistent with the particle kinetic energy being slightly lower at late times for the SN corrected scheme compared with the PR-DNS. The well ordering of the point-particle schemes is also found in the particle kinetic energy source term, namely that St corrected is better than SN uncorrected. The least accurate, as before, is the St uncorrected scheme which under-predicts the peak particle velocity–acceleration covariance as seen in the PR-DNS by almost 50 %.

Thus far, we have demonstrated validation of the point-particle method via the SN corrected implementation for Eulerian integral quantities (fluid kinetic energy and dissipation rate) as well as Lagrangian integral quantities (particle kinetic energy and dissipation rate). Finer appraisal of the accuracy of the point-particle schemes can be studied by examining the distribution of particle acceleration events. Probability density functions (PDFs) of particle acceleration for each of the schemes at three times are shown in figure 4. The corresponding sample mean and standard deviation of particle acceleration are presented in table 2. In examination of the PDF shapes and their moments, the SN corrected particle acceleration PDFs are in good agreement with the acceleration PDFs derived from the particle-resolved simulation at the same non-dimensional times. It is clear that the particle acceleration PDF is skewed towards higher accelerations in the particle-resolved simulation than any of the point-particle methods except for SN corrected. The SN corrected scheme shows good agreement in predicting the PDF mode and maximum particle acceleration, although the SN corrected scheme slightly over-predicts the mean and standard deviation of acceleration compared with the PR-DNS. Though the other point-particle schemes have the correct qualitative shape, they considerably underestimate the mean and standard deviation of acceleration as well as the maximum acceleration compared with those predicted by the PR-DNS simulation. Again the same ordering of the point-particle schemes is apparent, with St uncorrected showing the lowest level of agreement with the PR-DNS, followed by SN uncorrected. The St corrected scheme does a good job at predicting the location of the peak in the PR-DNS particle acceleration PDF, however, the St corrected PDF falls off too quickly, underpredicting the lower probability high acceleration events at early ($t\varepsilon_0^{(f)}/k_0^{(f)} = 0.54$) and intermediate ($t\varepsilon_0^{(f)}/k_0^{(f)} = 2.70$) times.

5. Discussion

What is remarkable about these observations is that employing a drag correlation (Schiller–Naumann) for isolated particles, which may be justified as predictive of the mean drag in a dilute suspension, shows excellent agreement not only for second

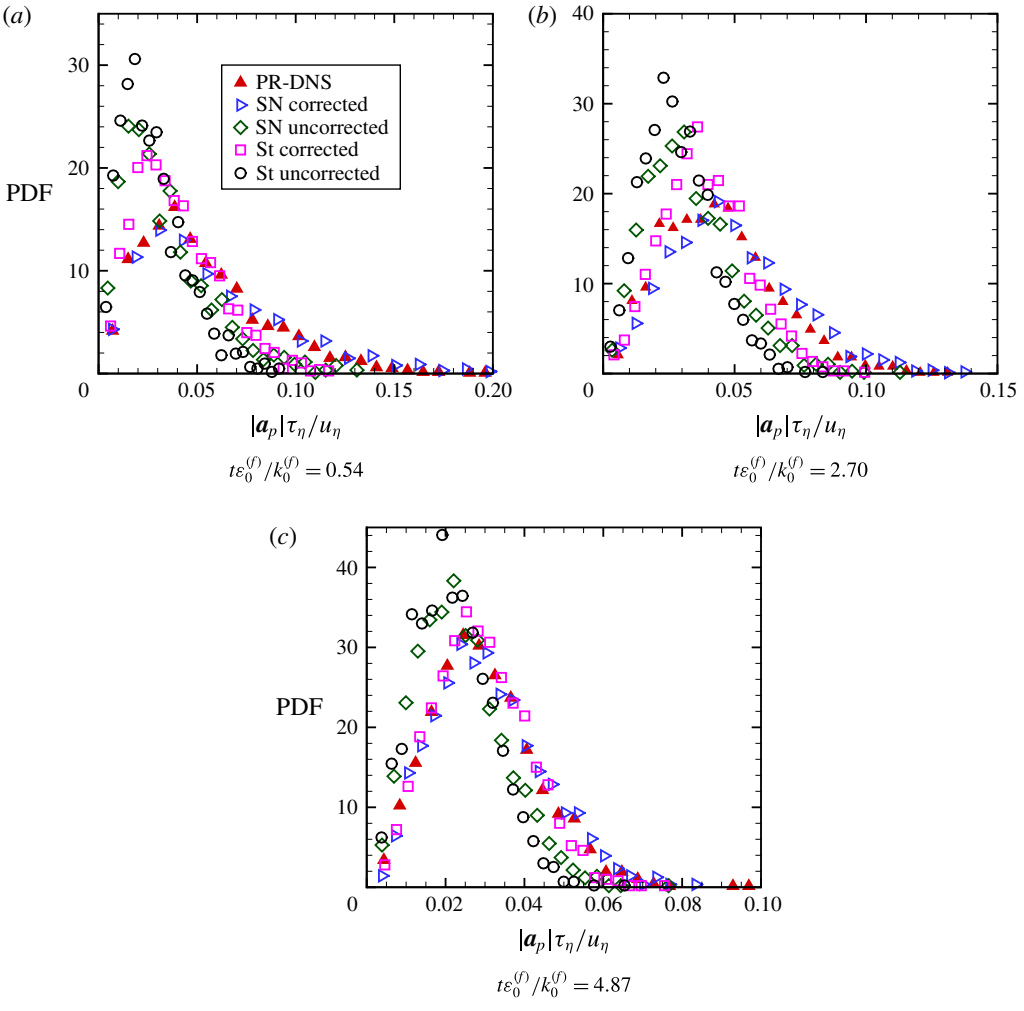

FIGURE 4. (Colour online) Particle acceleration PDFs at different times from particle-resolved simulation compared with different point-particle models.

moments such as $k^{(f)}$, $k^{(p)}$ and $\Pi^{(p)}$, but also in the distribution of particle acceleration events. The former is itself a surprising and unanticipated result. In other words, we find that point particles obeying a force model for an isolated sphere perform the correct work rate on the fluid in a dilute suspension, in a regime where the force model has empirical validity. The ability of the point-particle model to reproduce the acceleration–velocity covariance with acceptable accuracy, which is necessary to predict energetics, has to the best of the authors' knowledge never been shown before for a point-particle simulation.

What is more surprising however is that a force model for an isolated sphere can faithfully reproduce with reasonable accuracy the correct distribution of acceleration events as experienced by the dispersed phase in a dilute turbulent flow. Interpreted another way, this means there may be some validity to closing surface-integrated stress for a given particle in terms of quantities observed by that particle, namely the undisturbed velocity and the particle velocity, even when the particle experiences

nonlinear interactions with the fluid, and potentially other particles. Such a closure is on sound theoretical grounds in the low Reynolds number limit when a particle is isolated from others (Maxey & Riley 1983). It is not obvious that such a local relationship is not only possible, but has predictive power in a scenario where scale separation does not strictly exist: $Re_p = O(1)$, $d_p/\eta = O(1)$, and particles are close enough to see each other's disturbance flow (Stimson & Jeffrey 1926; Batchelor 1972; Batchelor & Green 1972). The latter point may be difficult to reconcile since the Schiller–Naumann correlation is established for isolated spheres. Scale separation or not, how could such a correlation for isolated spheres work in a system where the particles are close enough to see each other's disturbance flow? We discuss some plausible explanations below. Firstly, because the particle Stokes number is high, preferential concentration is relatively low, so that the bulk volume fraction can be used to infer a representative mean-free distance between particles. The mean inter-particle distance can be estimated using the Wigner–Seitz radius (Girifalco 2000), as $8(r_s/d_p)^3 = \phi^{-1}$, yielding $r_s = 5d_p$. Depending on the particle orientation, Stokesian arguments (Stimson & Jeffrey 1926; Batchelor 1972) would predict a reduction in the drag coefficient of the order of 10 % for a particle pair travelling at constant speed at a fixed separation equal to the Wigner–Seitz radius of the present study. The screening, at this distance, would not be considered a Faxén effect since the two spheres would be outside the distance where the $1/r^3$ term of each other's Stokeslet can be felt. Instead, the screening would be interpreted as the first particle obeying Stokes drag, with an undisturbed fluid velocity equal to the velocity of the fluid at the location of the first particle in the absence of both particles, plus the Stokeslet disturbance velocity created by the second particle at the location of the first particle, as if the first particle were not present. The same arguments apply for the undisturbed velocity at the location of the second particle. Koch (1990) has presented related analysis when the system is made up of a suspension of particles. In contrast, an isolated particle moving at a Reynolds number of unity in an otherwise quiescent flow would experience an enhancement in drag by exactly 15 % based on the Schiller–Naumann correlation as compared with Stokes' formula.

In the present problem there is therefore an apparent competition between drag enhancement due to fluid inertia and drag reduction due to particle–particle screening. However, there are other physical effects to consider. Firstly, it is worth noting that since the particle Reynolds numbers are sufficiently small in this study there should be no recirculation region present in particle wakes. Specifically, measurements of uniform flow over a sphere by Taneda (1956) suggest there is no recirculation region present for particle Reynolds numbers less than approximately 24. However, even in the presence of a turbulent flow, it is likely that fluctuations would be damped inside the Oseen distance at least for the order-unity particle Reynolds numbers encountered in this work. Secondly, the disturbance flows at finite Reynolds number are asymmetric and steeper near the particle than at zero Reynolds number (Ganguli & Lele 2017), a consequence of the minimum-energy dissipation theorem (Kim & Karrila 2005). Thirdly, the present problem is dealing with multiple moving particles so arguments based on two particles with a fixed separation are necessarily incomplete. We can however gain some insight into the hydrodynamics of many interacting particles by examining observations related to fixed arrays of spheres. Zick & Homsy (1982) examined laminar Stokes flow past different periodic arrangement of spheres. Their findings predict an enhancement of drag by approximately 21 % for $\phi = 0.001$ (the present case) with nominal differences based on the packing arrangement. Tenneti *et al.* (2011) examined flow past random arrays of spheres for

mean flow through Reynolds numbers in the range $Re_m \in [0.01, 300]$ and volume fractions in the range $\phi \in [0.1, 0.5]$. In that work, the initial velocity field is uniform, but the flow exhibits 'pseudo-turbulent' fluctuations owing to the interaction of the particle disturbance fields (Mehrabadi *et al.* 2015). Tenneti *et al.* (2011) propose a correlation which extends volume fraction corrections to the Schiller–Naumann correlation. The correlation takes the form

$$F(\phi, Re_m) = \frac{F^{SN}(Re_m)}{(1-\phi)^3} + \frac{5.81\phi}{(1-\phi)^3} + \frac{0.48\phi^{1/3}}{(1-\phi)^4} + \phi^3 Re_m \left(0.95 + \frac{0.61\phi^3}{(1-\phi)^3}\right). \quad (5.1)$$

Extrapolating this correlation to a volume fraction of 0.001 predicts a drag enhancement of approximately 5 % (at $Re_m = O(1)$), compared with an isolated particle obeying the Schiller–Naumann correlation.

These observations lead us to the conclusion that the effects of screening are of secondary importance in the drag correlation for this relatively dilute system and the primary contribution to the drag is owing to steady drag experienced by an isolated particle. Based on three scaling analyses (two isolated Stokesian particles, an infinite periodic array of Stokesian particles, and an infinite non-periodic array of finite Reynolds number particles) suggests the effects of screening are an order of magnitude smaller in their contribution to the total drag a particle experiences, compared with the contribution owing to the drag a particle would experience in isolation. For the present case this gives us some justification why the effects of screening – which were not explicitly modelled in the point-particle algorithm – were not necessary for validation against the particle-resolved algorithm, at least for integral statistics. To be clear, point particles do see disturbances created by other point particles, but these disturbances do not correspond to physical disturbances that could be compared pointwise to, for example, a Stokes flow around a sphere, in that limit. The nature of the disturbance flow is entirely dictated by the magnitude of the force and projection scheme used to transfer the Lagrangian force to the grid. Guarantees about the nature of the force are only possible in the Stokes regime, infinitely far from the particle, where the point-force solution is asymptotic to the Stokes stream function (Batchelor 1967). Nevertheless, the numerical tests performed by Horwitz & Mani (2016) suggest the contribution to the drag force experienced by one particle given other particles placed at the Wigner–Seitz radius for this problem, $r_s = 5d_p$, would be relatively small. Speculating, it is possible the effects of screening are suppressed owing to the transient configuration of the particle field in a flow which, though it induces a characteristic particle Reynolds number of $O(1)$, has no mean motion. Put another way, instantaneously in some regions of the flow, the particles are behaving as a swarm and are experiencing drag enhancement consistent with the observed increase in mean drag predicted by the studies that examined flow past an array of spheres. In other parts of the suspension, the particles are transiently isolated or only see a few neighbours, so that these particles experience drag reduction consistent with the scaling of the two-particle studies. The apparent contradiction of drag reduction versus drag enhancement for the two-particle based analysis versus the studies that examined flow past an array of spheres is likely owing to the difference in boundary conditions. In the former studies which consider two spheres, the disturbance flow is zero at infinite distances. The array configurations however employ periodic boundary conditions so that the disturbances do not decay to zero at an infinite distance from the spheres. Regardless of how we interpret 'boundary conditions' for particle neighbours in the present simulations, both types of

analysis suggest that for the present cases, the drag a particle experiences in isolation dominates the change in drag owing to the presence of one or more neighbours. However, while screening may be a second-order effect for accurate comparison of particle and fluid energetics, the observed differences in the particle acceleration PDFs suggest that particle screening may be more critical to accurately comparing these distributions. At higher volume fractions than that considered in this study, it would be especially prudent to directly model particle screening in point-particle simulation, using for instance the Langevin dynamics-based model of Tenneti *et al.* (2016) or the PIEP method (Akiki, Jackson & Balachandar 2017*a*; Akiki, Moore & Balachandar 2017*b*).

6. Conclusions

In this work, we performed a direct comparison of the PP-DNS and PR-DNS methods for the problem of decaying particle-laden homogeneous isotropic turbulence. We examined two cases, the first corresponds to low Stokes number (low mass loading) analogous to the conditions studied in Subramaniam *et al.* (2014). For this case, initializing particles with the local fluid velocity was found to be key in validating the PP-DNS statistics against the PR-DNS. Two PP-DNS implementations were considered. In each implementation, the particles were assumed to obey Stokes drag, however in one implementation, the slip velocity was calculated with the local disturbed fluid velocity (as has traditionally been done in the literature) and the second implementation incorporated an estimate of the undisturbed fluid velocity. In comparing fluid kinetic energy, dissipation rate, and particle kinetic energy, both PP-DNS implementations showed excellent agreement compared with the PR-DNS. The similarity in the prediction of the two PP-DNS models is attributed to the relatively small Stokes number. In this regime, it is likely that particles will tend to isotropically change their direction before a significant difference between the local disturbed and undisturbed fluid velocity can develop.

Having successfully validated the PP-DNS against the PR-DNS for the low mass loading case, we examined a more challenging problem by increasing the mass loading of the system. Here, the suppression of the velocity mismatch in the initial condition was not sufficient for the statistics obtained in the PP-DNS and PR-DNS to agree. In this problem, the high Stokes number of the particles led to a relatively high slip velocity compared to the previous case. The fluid dissipation increased substantially over the unladen fluid owing to the additional work rate necessary to slow down the particles. For this problem, the model form of acceleration and its numerical implementation were both critical to validating the particle and fluid statistics. The enhanced slip velocity (Reynolds number) of the particles meant that the inertial contribution to drag was non-negligible. The Schiller–Naumann correlation was adopted as a model for drag enhancement at finite Reynolds number. However, it was also found that modelling the undisturbed fluid velocity was as critical to successful validation as the choice of drag model. When the Schiller–Naumann correlation was combined with an estimate for the undisturbed fluid velocity, particle and fluid kinetic energy as well as the sources that create them showed excellent agreement between the PR-DNS and PP-DNS simulations. Remarkably however, it was found that point particles obeying Stokes drag computed using the undisturbed fluid velocity implied more accurate statistics than did point particles obeying the Schiller–Naumann correlation computed using the disturbed fluid velocity. Stokesian point particles using the disturbed fluid velocity were the least accurate compared with

the PR-DNS. The same trend was found when examining the one-time distribution of particle acceleration events over the history of the decay. The acceleration PDFs for SN corrected point particles at all times were in good agreement with the acceleration PDFs from the PR-DNS. Stokes uncorrected particle acceleration PDFs showed the lowest level of agreement compared with the particle acceleration events predicted by the PR-DNS. Though the volume fraction of the system was relatively dilute, previous studies suggested the effect of screening would be non-negligible in this system. The reason that such effects did not seem to have an $O(1)$ impact on the present results is that the effect of screening may increase or decrease a particle's acceleration depending on the precise configuration of other particles in a given particle's neighbourhood. We suspect that these competing effects statistically cancelled which is why the results of SN corrected scheme and those of the PR-DNS showed good agreement.

The fact that a simple steady drag model for the particle acceleration was effective in prediction of both energy and acceleration statistics suggests that the point-particle model has predictive capability, and serves as a considerably less computationally expensive methodology compared with PR-DNS. Still, the present study is limited to a small region of parameter space. Specifically, the Reynolds number was relatively low, $R_{\lambda_0} \approx 27$, so it would be prudent to examine whether the present conclusions hold at higher Reynolds number. The present work was also focused on the relatively simple problem of decaying homogeneous turbulence; it would be interesting to explore comparisons of this type in inhomogeneous and wall-bounded turbulent flows. In addition, the Stokes number in this study was varied at constant particle size while varying the density ratio. We believe the comparison between PP-DNS and PR-DNS would have shown similar agreement if instead the Stokes number was varied at constant density ratio by decreasing the particle size, since this would be a regime where the PP-DNS becomes increasingly asymptotically valid. However, the computational resources required to perform PR-DNS in that regime becomes increasingly demanding. If instead, the Stokes number is increased at constant density ratio by increasing the particle size, we feel the present observations, namely that the appropriate drag model and incorporation of the undisturbed fluid velocity are necessary for accurate comparison, would be germane in regimes where $d_p/\eta > 1$. However, with increasing particle size, it will be especially important to also consider other contributions to the particle equation of motion in the point-particle simulations, including added mass, history, fluid acceleration, and lift. Due to the low number of particles in this study, we were not able to accurately extract more sensitive quantities such as the particle radial distribution function. Horwitz & Mani (2018) have shown that incorporation of the undisturbed fluid velocity can change predictions of preferential concentration, so it would be of value to carry out future studies to see how these multi-point quantities compare between PP-DNS and PR-DNS. More studies which directly compare PP-DNS and PR-DNS should also be undertaken to test the validity of the point-particle method in other flow regimes.

Acknowledgements

This work was funded in part by the United States Department of Energy through the Predictive Science Academic Alliance Program 2 (PSAAP2) at Stanford University under grant no. DE-NA0002373, by a Department of Energy grant DE-FC26-07NT43098 through the National Energy Technology Laboratory and by a National Science Foundation grant CBET 1134500. In addition, J.H. has been

supported by the National Science Foundation Graduate Research Fellowship under grant no. DGE-114747. Any opinion, findings, and conclusions or recommendations expressed in this material are those of the authors and do not necessarily reflect the views of the National Science Foundation.

Appendix A. Derivation of total energy equation for point-particle method

In this section, we derive the energy equations implied by the point-particle model equations. Beginning with the particle momentum equation for the ith particle:

$$m_p \frac{\mathrm{d}\boldsymbol{V}_i}{\mathrm{d}t} = \boldsymbol{F}_{i,pp}. \tag{A 1}$$

In (A 1), $\boldsymbol{F}_{i,pp}$ is the total force acting on particle i. Contracting (A 1) with the particle velocity and summing over all particles yields:

$$m_p \frac{\mathrm{d}}{\mathrm{d}t}\frac{1}{N_p}\sum_{i=1}^{N_p}\frac{1}{2}\boldsymbol{V}_i\cdot\boldsymbol{V}_i = \frac{1}{N_p}\sum_{i=1}^{N_p}\boldsymbol{F}_{i,pp}\cdot\boldsymbol{V}_i. \tag{A 2}$$

Using the definition of particle kinetic energy $k^{(p)} \equiv (1/N_p)\sum_{i=1}^{N_p}(1/2)\boldsymbol{V}_i\cdot\boldsymbol{V}_i$, dividing through by particle mass and multiplying by $\rho^{(p)}$ and ϕ yields:

$$\frac{\mathrm{d}}{\mathrm{d}t}\phi\rho^{(p)}k^{(p)} = \rho^{(p)}\frac{N_p\dfrac{\pi d_p^3}{6}}{V}\frac{1}{N_p}\sum_{i=1}^{N_p}\boldsymbol{A}_{i,pp}\cdot\boldsymbol{V}_i. \tag{A 3}$$

In (A 3), $\boldsymbol{A}_{i,pp}$ is the acceleration of the ith particle. Simplifying the above yields:

$$\frac{\mathrm{d}}{\mathrm{d}t}\phi\rho^{(p)}k^{(p)} = \frac{1}{V}\sum_{i=1}^{N_p}\boldsymbol{F}_{i,pp}\cdot\boldsymbol{V}_i = \Pi_{pp}^{(p)}, \tag{A 4}$$

which is the expression given in (2.12).

Next we derive the fluid energy from the point-particle equations. Beginning with the Navier–Stokes equations augmented by the point-particle force:

$$\rho^{(f)}\frac{\partial\boldsymbol{u}^{(f)}}{\partial t} + \rho^{(f)}\boldsymbol{\nabla}\cdot(\boldsymbol{u}^{(f)}\boldsymbol{u}^{(f)}) = -\boldsymbol{\nabla}p + \mu^{(f)}\nabla^2\boldsymbol{u}^{(f)} - \frac{1}{V_{cell}}\sum_{i=1}^{N_p}\boldsymbol{F}_{i,pp}\mathcal{P}(\delta(\boldsymbol{X}_i-\boldsymbol{x})). \tag{A 5}$$

Contracting (A 5) with the fluid velocity and integrating over the volume we have:

$$\begin{aligned}\frac{\mathrm{d}}{\mathrm{d}t}\rho^{(f)}\frac{1}{V}\int_V\frac{1}{2}\boldsymbol{u}^{(f)}\boldsymbol{u}^{(f)}\,\mathrm{d}V \;=\; &\frac{1}{V}\int_V\mu^{(f)}\boldsymbol{u}^{(f)}\nabla^2\boldsymbol{u}^{(f)}\,\mathrm{d}V \\ &-\frac{1}{V}\int_V\frac{1}{V_{cell}}\sum_{i=1}^{N_p}\boldsymbol{u}^{(f)}\cdot\boldsymbol{F}_{i,pp}\mathcal{P}(\delta(\boldsymbol{X}_i-\boldsymbol{x}))\,\mathrm{d}V.\end{aligned} \tag{A 6}$$

In the above equation, we have made use of the fact that convective and pressure work terms can be placed in divergence form discretely, consistent with the staggered formulation of the point-particle solver. Using the definition of fluid kinetic energy (in

this case the mean fluid velocity is zero) $k_{pp}^{(f)} \equiv (1/V)\int_V (1/2)\boldsymbol{u}^{(f)}\boldsymbol{u}^{(f)}\,\mathrm{d}V$, dissipation rate $-\varepsilon_{pp}^{(f)} \equiv (1-\phi)(1/V)\int_V \mu^{(f)}\boldsymbol{u}^{(f)}\nabla^2\boldsymbol{u}^{(f)}\,\mathrm{d}V$ and the fact that the projection operator $\mathcal{P}(\cdot)$ is conservative, the point-particle fluid energy equation becomes:

$$\frac{\mathrm{d}}{\mathrm{d}t}(1-\phi)\rho^{(f)}k_{pp}^{(f)} = -\varepsilon_{pp}^{(f)} - (1-\phi)\frac{1}{V}\sum_{i=1}^{N_p}\boldsymbol{u}^{(f)}(\boldsymbol{X}_i)\cdot\boldsymbol{F}_{i,pp}. \tag{A 7}$$

The final term in (A 7) may be recognized as the fluid to particle interphase energy exchange term (2.11). Combining (A 4) and (A 7), and using the definition of the mixture energy, $e_{pp}^{m} = (1-\phi)\rho^{(f)}k_{pp}^{(f)} + \phi\rho^{(p)}k^{(p)}$, the mixture energy equation for point particles is:

$$\frac{\mathrm{d}e_{pp}^{(m)}}{\mathrm{d}t} = -\varepsilon_{pp}^{(f)} + \frac{1}{V}\sum_{i=1}^{N_p}\boldsymbol{F}_{i,pp}\cdot(\boldsymbol{V}_i - \boldsymbol{u}^{(f)}(\boldsymbol{X}_i)) + \phi\frac{1}{V}\sum_{i=1}^{N_p}\boldsymbol{u}^{(f)}(\boldsymbol{X}_i)\cdot\boldsymbol{F}_{i,pp}. \tag{A 8}$$

The final term in (A 8) can be re-written as:

$$\phi\frac{1}{V}\sum_{i=1}^{N_p}\boldsymbol{u}^{(f)}(\boldsymbol{X}_i)\cdot\boldsymbol{F}_{i,pp} = \phi\frac{m_pN_p}{V}\left(\frac{1}{N_p}\right)\sum_{i=1}^{N_p}\boldsymbol{u}_i^{(f)}\cdot\boldsymbol{A}_{i,pp} = \rho_p\phi^2\{\boldsymbol{u}_i^{(f)}\cdot\boldsymbol{A}_{i,pp}\}_{N_p} = O(\phi^2). \tag{A 9}$$

Similarly, the second term on the right-hand side of (A 8) can be written as:

$$\frac{1}{V}\sum_{i=1}^{N_p}\boldsymbol{F}_{i,pp}\cdot(\boldsymbol{V}_i - \boldsymbol{u}^{(f)}(\boldsymbol{X}_i)) = \rho_p\phi\{(\boldsymbol{V}_i - \boldsymbol{u}_i^{(f)})\cdot\boldsymbol{A}_{i,pp}\}_{N_p} = O(\phi). \tag{A 10}$$

The previous analysis justifies the neglect of the final term in (A 8) when reporting (3.14) and (3.15), which are written in the dilute limit. For completeness however, all of the terms on the right-hand side of (A 8) were included when comparing fluid dissipation rate in the PP-DNS to the PR-DNS.

Appendix B. Consideration of collisions in the point-particle method

Here we consider the effect of collisions on the predictions of the point-particle method. We had originally neglected collisions owing to the low volume fraction of the suspension. However, to establish a better comparison with the PR-DNS simulation, we have re-run the $St = 100$ set-up for both the SN uncorrected and SN corrected point-particle models including the effects of collision. We have incorporated the same soft-sphere collision model into the point-particle code as was used in the particle-resolved code. To avoid some issues related to numerical stiffness since the spring constant used in the PR-DNS was very large and the PP-DNS simulations use explicit time stepping, we have reduced the spring constant in the PP-DNS. The spring constant used in the PP-DNS simulations was chosen to yield a collision time much smaller than all fluid time scales so that while the dimensional collision time is different between the PP-DNS and the PR-DNS, there should be negligible effect of the collision time on the dynamics of the particles during non-collision events.

In figure 5, we show that incorporation of collisions shows no significant difference in the prediction of the point-particle model. No discernible change in the dissipation rate predicted by the SN corrected scheme is evident when collisions are added, as

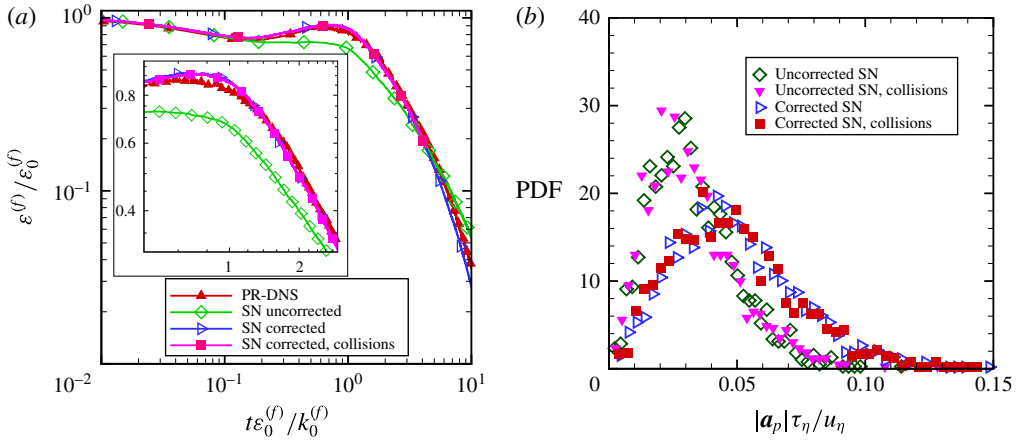

FIGURE 5. (Colour online) Effect of collisions on (*a*) dissipation rate, and (*b*) particle acceleration PDF at $t\varepsilon_0^{(f)}/k_0^{(f)} = 2.70$.

	$\lvert\boldsymbol{a}_p\rvert$	$\sigma_{\lvert\boldsymbol{a}_p\rvert}$
SN corrected, collisions	0.048	0.024
SN corrected	0.049	0.024
SN uncorrected, collisions	0.032	0.017
SN uncorrected	0.033	0.017

TABLE 3. Effect of collisions on mean and standard deviation of particle acceleration for PP-DNS for $St_0 = 100$, $t\varepsilon_0^{(f)}/k_0^{(f)} = 2.70$. These quantities are normalized by the initial Kolmogorov velocity scale u_η and time scale τ_η.

shown in figure 5(*a*). In figure 5(*b*), we also see that collisions show no significant effect on the distribution of acceleration events for either point-particle scheme. In examining table 3, the mean and standard deviation of particle acceleration are essentially unchanged whether or not collisions are incorporated. These results suggest the assumptions of neglecting collisions in the point-particle simulations was justified for the present case. Furthermore, these observations provide further evidence that the differences between the statistics of PP-DNS simulations and PR-DNS simulations are primarily owing to the choice of drag formulation and the modelling of the undisturbed fluid velocity. In other regimes, it is expected that collisions could play a central role in comparison between PR-DNS and PP-DNS methodologies. The collision model presented here is non-dissipative, so the effect on energetics is expected to be negligible. In addition, the low volume fraction of the system kept the number of collisions relatively low. For illustration, both point-particle methods predicted each particle experienced an average of approximately one collision over the course of the simulation. In other words, although most, if not all, of the particle population collides at some point, each particle spends most of its time in free flight.

Appendix C. Effect of grid resolution on PR-DNS results

The particle-resolved direct numerical simulation (PR-DNS) approach in this study is based on PUReIBM, which has been shown to be convergent and capable of

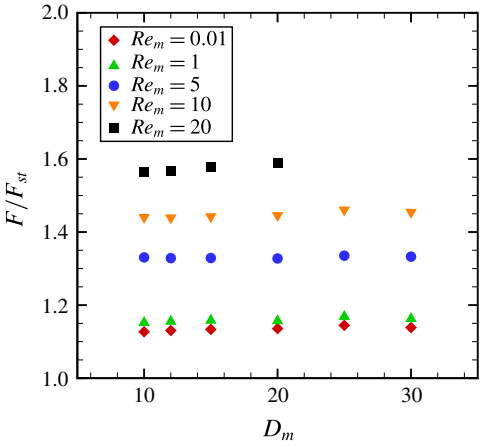

FIGURE 6. (Colour online) Convergence of the mean drag force on a particle normalized by the Stokes drag force $F_{St} = 3\pi d_p\, \mu^{(f)}(1-\phi)\, |\langle \boldsymbol{u}_p \rangle - \langle \boldsymbol{u}_f \rangle|$ with increasing grid resolution in a simple cubic configuration at $\phi = 0.001$ for different mean-slip Reynolds numbers ($Re_m = d_p\,(1-\phi)\,|\langle \boldsymbol{u}_p \rangle - \langle \boldsymbol{u}_f \rangle|/\nu^{(f)}$).

reproducing established analytical and numerical results (Tenneti *et al.* 2011, 2013; Mehrabadi *et al.* 2015; Sun *et al.* 2015; Mehrabadi *et al.* 2016*a*). Nevertheless, in the aforementioned references, the simulations have been performed for much higher solid-phase volume fractions ($\phi \geqslant 0.1$) than what has been considered in the present study which is $\phi = 0.001$. To investigate the accuracy of the grid resolution for our PR-DNS calculations, we first computed the local particle Reynolds number for each particle in our PR-DNS for an early instance of the simulation, and then generated the PDF of the local particle Reynolds number. This quantification showed that the mean and maximum particle Reynolds number were both $O(1)$. Correspondingly, we set up a convergence analysis for a simple cubic configuration with a range of mean-slip Reynolds numbers ($0.01 \leqslant Re_m \leqslant 20$) and particle diameter resolution $D_m = d_p/\Delta x$ ($10 \leqslant D_m \leqslant 30$). As shown in figure 6, the drag force on the particle is almost invariant with respect to the grid resolution at such a low solid-phase volume fraction. Consequently, the chosen grid resolution ($d_p = 12\Delta x$) is adequate for the PR-DNS calculations in the current study.

REFERENCES

AKIKI, G., JACKSON, T. L. & BALACHANDAR, S. 2017*a* Pairwise interaction extended point-particle model for a random array of monodisperse spheres. *J. Fluid Mech.* **813**, 882–928.

AKIKI, G., MOORE, W. C. & BALACHANDAR, S. 2017*b* Pairwise-interaction extended point-particle model for particle-laden flows. *J. Comput. Phys.* **351**, 329–357.

BAGCHI, P. & BALACHANDAR, S. 2003 Effect of turbulence on the drag and lift of a particle. *Phys. Fluids* **15** (11), 3496–3513.

BALACHANDAR, S. & EATON, J. K. 2010 Turbulent dispersed multiphase flow. *Annu. Rev. Fluid Mech.* **42**, 111–133.

BALACHANDAR, S. & MAXEY, M. R. 1989 Methods for evaluating fluid velocities in spectral simulations of turbulence. *J. Comput. Phys.* **83**, 96–125.

BASSET, A. B. 1888 *A Treatise on Hydrodynamics: With Numerous Examples*, vol. 2. Cambridge University Press.

BATCHELOR, G. K. 1967 *An Introduction to Fluid Dynamics*. Cambridge University Press.

BATCHELOR, G. K. 1972 Sedimentation in a dilute dispersion of spheres. *J. Fluid Mech.* **52**, 245–268.

BATCHELOR, G. K. & GREEN, J. T. 1972 The hydrodynamic interaction of two small freely-moving spheres in a linear flow field. *J. Fluid Mech.* **56** (2), 375–400.

BOIVIN, M., SIMONIN, O. & SQUIRES, K. D. 1998 Direct numerical simulation of turbulence modulation by particles in isotropic turbulence. *J. Fluid Mech.* **275**, 235–263.

BOKKERS, G. A., ANNALAND, M. V. S. & KUIPERS, J. A. M. 2004 Mixing and segregation in a bidisperse gas–solid fluidised bed: a numerical and experimental study. *Powder Technol.* **140**, 176–186.

BOUSSINESQ, J. 1885 Sur la résistance qu'oppose un liquide indéfini en repos, sans pesanteur, au mouvement varié d'une sphère solide qu'il mouille sur toute sa surface, quand les vitesses restent bien continues et assez faibles pour que leurs carrés et produits soient négligeables. *C. R. Acad. Sci. Paris* **100**, 935–937.

BURTON, T. M. & EATON, J. K. 2005 Fully resolved simulations of particle-turbulence interaction. *J. Fluid Mech.* **545**, 67–111.

CALZAVARINI, E., VOLK, R., BOURGOIN, M., LEVEQUE, E., PINTON, J. F. & TOSCHI, F. 2009 Acceleration statistics of finite-sized particles in turbulent flow: the role of Faxén forces. *J. Fluid Mech.* **630**, 179–189.

CATE, A. T., DERKSEN, J. J., PORTELA, L. M. & VAN DEN AKKER, H. E. A. 2004 Fully resolved simulations of colliding monodisperse spheres in forced isotropic turbulence. *J. Fluid Mech.* **519**, 233–271.

CHOUIPPE, A. & UHLMANN, M. 2015 Forcing homogeneous turbulence in direct numerical simulation of particulate flow with interface resolution and gravity. *Phys. Fluids* **27** (12), 123301.

CLIFT, R., GRACE, J. R. & WEBER, M. E. 1978 *Bubbles, Drops and Particles*. Academic.

COIMBRA, C. F. M. & RANGEL, R. H. 1998 General solution of the particle momentum equation in unsteady Stokes flows. *J. Fluid Mech.* **370**, 53–72.

CORRSIN, S. & LUMLEY, J. 1956 On the equation of motion for a particle in turbulent fluid. *Appl. Sci. Res.* A **6**, 114–116.

CUNDALL, P. A. & STRACK, O. D. L. 1979 A discrete numerical model for granular assemblies. *Geotechnique* **29**, 47–65.

DAITCHE, A. 2015 On the role of the history force for inertial particles in turbulence. *J. Fluid Mech.* **782**, 567–593.

DREW, D. A. & PASSMAN, S. L. 1998 *Theory of Multicomponent Fluids*. Springer.

ELGHOBASHI, S. & TRUESDELL, G. C. 1992 Direct simulation of particle dispersion in a decaying isotropic turbulence. *J. Fluid Mech.* **242**, 655–700.

ELGHOBASHI, S. E. & TRUESDELL, G. C. 1993 On the two-way interaction between homogeneous turbulence and dispersed solid particles. I: Turbulence modification. *Phys. Fluids* A **5**, 1790–1801.

FAN, R., MARCHISIO, D. L. & FOX, R. O. 2004 Application of the direct quadrature method of moments to polydisperse gas–solid fluidized beds. *Powder Technol.* **139** (1), 7–20.

FAXÉN, V. H. 1922 Der widerstand gegen die bewegung einer starren kugel in einer zahen flussigkeit, die zwischen zwei parallelen ebenen wanden eingeschlossen ist. *Ann. Phys.* **373** (10), 89–119.

FERRANTE, A. & ELGHOBASHI, S. 2003 On the physical mechanisms of two-way coupling in particle-laden isotropic turbulence. *Phys. Fluids* **15** (2), 315–329.

FRANKEL, A., POURANSARI, H., COLETTI, F. & MANI, A. 2016 Settling of heated particles in homogeneous turbulence. *J. Fluid Mech.* **792**, 869–893.

GANGULI, S. & LELE, S. 2017 Importance of variable density and non-Boussinesq effects on the drag of spherical particles. In *70th Annual Meeting of the APS Division of Fluid Dynamics, Denver, CO*. American Physical Society.

GAO, H., LI, H. & WANG, L.-P. 2013 Lattice Boltzmann simulation of turbulent flow laden with finite-size particles. *Comput. Math. Appl.* **65** (2), 194–210.

GARG, R., TENNETI, S., MOHD-YUSOF, J. & SUBRAMANIAM, S. 2011 Direct numerical simulation of gas–solids flow based on the immersed boundary method. In *Computational Gas-Solids*

Flows and Reacting Systems: Theory, Methods and Practice (ed. S. Pannala, M. Syamlal & T. J. O'Brien), pp. 245–276. IGI Global.

GATIGNOL, R. 1983 The Faxén formulae for a rigid sphere in an unsteady non-uniform stokes flow. *Journal de mécanique théorique et appliquée* **1**, 143–160.

GIRIFALCO, L. A. 2000 *Statistical Mechanics of Solids*. Oxford University Press.

GOLDSCHMIDT, M. J. V., LINK, J. M., MELLEMA, S. & KUIPERS, J. A. M. 2003 Digital image analysis measurements of bed expansion and segregation dynamics in dense gas–solid fluidized beds. *Powder Technol.* **138**, 135–159.

GUALTIERI, P., PICANO, F., SARDINA, G. & CASCIOLA, C. M. 2015 Exact regularized point particle method for multiphase flows in the two-way coupling regime. *J. Fluid Mech.* **773**, 520–561.

HOMANN, H. & BEC, J. 2010 Finite-size effects in the dynamics of neutrally buoyant particles in turbulent flow. *J. Fluid Mech.* **651**, 81–91.

HORWITZ, J. & MANI, A. 2015 Simulations of decaying turbulence laden with particles: how are statistics affected by two-way coupling numerical scheme? In *68th Annual Meeting of the APS Division of Fluid Dynamics, Boston, Massachusetts*. American Physical Society.

HORWITZ, J. A. K. & MANI, A. 2016 Accurate calculation of stokes drag for point-particle tracking in two-way coupled flows. *J. Comput. Phys.* **318**, 85–109.

HORWITZ, J. A. K. & MANI, A. 2018 Correction scheme for point-particle models applied to a nonlinear drag law in simulations of particle-fluid interaction. *Intl J. Multiphase Flow* **101**, 74–84.

HORWITZ, J. A. K., RAHMANI, M., GERACI, G., BANKO, A. J. & MANI, A. 2016 Two-way coupling effects in particle-laden turbulence: how particle-tracking scheme affects particle and fluid statistics. In *9th International Conference on Multiphase Flow, Firenze*.

IRELAND, P. J. & DESJARDINS, O. 2017 Improving particle drag predictions in euler-lagrange simulations with two-way coupling. *J. Comput. Phys.* **338**, 405–430.

KIDANEMARIAM, A. G., CHAN-BRAUN, C., DOYCHEV, T. & UHLMANN, M. 2013 Direct numerical simulation of horizontal open channel flow with finite-size, heavy particles at low solid volume fraction. *New J. Phys.* **15** (2), 025031.

KIGER, K. T. & PAN, C. 2000 PIV technique for the simultaneous measurement of dilute two-phase flows. *Trans. ASME J. Fluids Engng* **122** (4), 811–818.

KIM, J. & MOIN, P. 1985 Application of a fractional-step method to incompressible Navier–Stokes equations. *J. Comput. Phys.* **59**, 308–323.

KIM, S. & KARRILA, S. J. 2005 *Microhydrodynamics: Principles and Selected Applications*. Butterworth-Heinemann.

KOCH, D. L. 1990 Kinetic theory for a monodisperse gas–solid suspension. *Phys. Fluids* A **2**, 1711–1723.

LEE, S. L. & DURST, F. 1982 On the motion of particles in turbulent duct flows. *Intl J. Multiphase Flow* **8** (2), 125–146.

LING, Y., PARMAR, M. & BALACHANDAR, S. 2013 A scaling analysis of added-mass and history forces and their coupling in dispersed multiphase flows. *Intl J. Multiphase Flow* **57**, 102–114.

LOVALENTI, P. M. & BRADY, J. F. 1993 The hydrodynamic force on a rigid particle undergoing arbitrary time-dependent motion at small Reynolds number. *J. Fluid Mech.* **256**, 561–605.

LUCCI, F., FERRANTE, A. & ELGHOBASHI, S. 2011 Is Stokes number an appropriate indicator for turbulence modulation by particles of Taylor-length-scale size? *Phys. Fluids* **23** (2), 025101.

MAXEY, M. R. & RILEY, J. J. 1983 Equation of motion for a small rigid sphere in a uniform flow. *Phys. Fluids* **26** (4), 883–889.

MEHRABADI, M., MURPHY, E. & SUBRAMANIAM, S. 2016*a* Development of a gas–solid drag law for clustered particles using particle-resolved direct numerical simulation. *Chem. Engng Sci.* **152**, 199–212.

MEHRABADI, M. & SUBRAMANIAM, S. 2017 Mechanism of kinetic energy transfer in homogeneous bidisperse gas–solid flow and its implications for segregation. *Phys. Fluids* **29**, 020714.

MEHRABADI, M., TENNETI, S., GARG, R. & SUBRAMANIAM, S. 2015 Pseudo-turbulent gas-phase velocity fluctuations in homogeneous gas–solid flow: fixed particle assemblies and freely evolving suspensions. *J. Fluid Mech.* **770**, 210–246.

MEHRABADI, M., TENNETI, S. & SUBRAMANIAM, S. 2016*b* Importance of the fluid-particle drag model in predicting segregation in bidisperse gas–solid flow. *Intl J. Multiphase Flow* **86**, 99–114.

MOHD-YUSOF, J. 1996 Interaction of massive particles with turbulence. PhD thesis, Cornell University.

NASO, A. & PROSPERETTI, A. 2010 The interaction between a solid particle and a turbulent flow. *New J. Phys.* **12** (3), 033040.

OAKLEY, T. R., LOTH, E. & ADRIAN, R. J. 1997 A two-phase cinematic PIV method for bubbly flows. *Trans. ASME J. Fluids Engng* **119** (3), 707–712.

OLIVIERI, S., PICANO, F., SARDINA, G., IUDICONE, D. & BRANDT, L. 2014 The effect of the basset history force on particle clustering in homogeneous and isotropic turbulence. *Phys. Fluids* **26**, 041704.

OZEL, A., DE MOTTAA, J. C. B., ABBAS, M., FEDEA, P., MASBERNAT, O., VINCENT, S., ESTIVALEZES, J. L. & SIMONIN, O. 2017 Particle resolved direct numerical simulation of a liquid–solid fluidized bed: comparison with experimental data. *Intl J. Multiphase Flow* **89**, 228–240.

PAI, M. G. & SUBRAMANIAM, S. 2009 A comprehensive probability density function formalism for multiphase flows. *J. Fluid Mech.* **628**, 181–228.

PARMAR, M., HASELBACHER, A. & BALACHANDAR, S. 2012 Equation of motion for a sphere in non-uniform compressible flows. *J. Fluid Mech.* **699**, 352–375.

POPE, S. B. 2000 *Turbulent Flows*. Cambridge University Press.

POURANSARI, H., MORTAZAVI, M. & MANI, A. 2015 Parallel variable-density particle-laden turbulence simulation. *Annu. Res. Briefs* **2015**, 43–54.

READE, W. C. & COLLINS, L. R. 2000 Effect of preferential concentration on turbulent collision rates. *Phys. Fluids* **12** (10), 2530–2540.

RILEY, J. J. & PATTERSON, G. S. 1974 Diffusion experiments with numerically integrated isotropic turbulence. *Phys. Fluids* **17** (2), 292–297.

ROGALLO, R. S. 1981 Numerical experiments in homogeneous turbulence. *NASA Tech. Rep.* 81835.

ROGERS, C. B. & EATON, J. K. 1991 The effect of small particles on fluid turbulence in a flat plate, turbulent boundary layer in air. *Phys. Fluids* **3** (5), 928–937.

SATO, Y., HISHIDA, K. & MAEDA, M. 1996 Effect of dispersed phase on modification of turbulent flow in a wall jet. *Trans. ASME J. Fluids Engng* **118** (2), 307–315.

SCHNEIDERS, L., MEINKE, M. & SCHRODER, W. 2016 On the accuracy of Lagrangian point-mass models for heavy nonspherical particles in isotropic turbulence. *Fuel* **201**, 2–14.

SQUIRES, K. D. & EATON, J. K. 1990 Particle response and turbulence modification in isotropic turbulence. *Phys. Fluids* A **2** (7), 292–297.

SQUIRES, K. D. & EATON, J. K. 1991*a* Measurements of particle dispersion obtained from direct numerical simulations of isotropic turbulence. *J. Fluid Mech.* **226**, 1–35.

SQUIRES, K. D. & EATON, J. K. 1991*b* Preferential concentration of particles by turbulence. *Phys. Fluids* A **3**, 1169–1178.

STIMSON, M. & JEFFREY, G. G. 1926 The motion of two spheres in a viscous fluid. *Proc. R. Soc. Lond.* A **111** (757), 110–116.

STOKES, G. G. 1850 On the effect of the inertial friction of fluids on the motion of pendulums. *Trans. Camb. Phil. Soc.* **9**, 1–86.

SUBRAMANIAM, S., MEHRABADI, M., HORWITZ, J. & MANI, A. 2014 Developing improved lagrangian point particle models of gas–solid flow from particle-resolved direct numerical simulation. In *Studying Turbulence Using Numerical Simulation Databases–XV, Proceedings of the CTR 2014 Summer Program*, pp. 5–14. Center for Turbulence Research, Stanford University.

SUN, B., TENNETI, S. & SUBRAMANIAM, S. 2015 Modeling average gas–solid heat transfer using particle-resolved direct numerical simulation. *Intl J. Heat Mass Transfer* **86**, 898–913.

SUN, B., TENNETI, S., SUBRAMANIAM, S. & KOCH, D. L. 2016 Pseudo-turbulent heat flux and average gas-phase conduction during gas–solid heat transfer: flow past random fixed particle assemblies. *J. Fluid Mech.* **798**, 299–349.

SUNDARAM, S. & COLLINS, L. R. 1996 Numerical considerations in simulating a turbulent suspension of finite-volume particles. *J. Comput. Phys.* **124**, 337–350.

SUNDARAM, S. & COLLINS, L. R. 1997 Collision statistics in an isotropic particle-laden turbulent suspension. Part 1. Direct numerical simulations. *J. Fluid Mech.* **335**, 75–109.

SUNDARAM, S. & COLLINS, L. R. 1999 A numerical study of the modulation of isotropic turbulence by suspended particles. *J. Fluid Mech.* **379**, 105–143.

TANEDA, S. 1956 Experimental investigation of the wake behind a sphere at low Reynolds numbers. *J. Phys. Soc. Japan* **11** (10), 1104–1108.

TENNETI, S., GARG, R., HRENYA, C. M., FOX, R. O. & SUBRAMANIAM, S. 2010 Direct numerical simulation of gas–solid suspensions at moderate Reynolds number: quantifying the coupling between hydrodynamic forces and particle velocity fluctuations. *Powder Technol.* **203** (1), 57–69.

TENNETI, S., GARG, R. & SUBRAMANIAM, S. 2011 Drag law for monodisperse gas–solid systems using particle-resolved direct numerical simulation of flow past fixed assemblies of spheres. *Intl J. Multiphase Flow* **37**, 1072–1092.

TENNETI, S., MEHRABADI, M. & SUBRAMANIAM, S. 2016 Stochastic Lagrangian model for hydrodynamic acceleration of inertial particles in gas–solid suspensions. *J. Fluid Mech.* **788**, 695–729.

TENNETI, S. & SUBRAMANIAM, S. 2014 Particle-resolved direct numerical simulation for gas–solid flow model development. *Annu. Rev. Fluid Mech.* **46** (1), 199–230.

TENNETI, S., SUN, B., GARG, R. & SUBRAMANIAM, S. 2013 Role of fluid heating in dense gas–solid flow as revealed by particle-resolved direct numerical simulation. *Intl J. Heat Mass Transfer* **58** (1), 471–479.

TRUESDELL, G. C. & ELGHOBASHI, S. 1994 On the two-way interaction between homogeneous turbulence and dispersed solid particles. II. Particle dispersion. *Phys. Fluids* **6** (3), 1405–1407.

UHLMANN, M. 2008 Interface-resolved direct numerical simulation of vertical particulate channel flow in the turbulent regime. *Phys. Fluids* **20** (5), 053305.

WANG, L.-P., AYALA, O., GAO, H., ANDERSEN, C. & MATHEWS, K. L. 2014 Study of forced turbulence and its modulation by finite-size solid particles using the lattice Boltzmann approach. *Comput. Maths Applics.* **67** (2), 363–380.

WANG, L.-P. & MAXEY, M. R. 1993 Settling velocity and concentration distribution of heavy particles in homogeneous isotropic turbulence. *Phys. Fluids* **256**, 27–68.

XU, Y. & SUBRAMANIAM, S. 2007 Consistent modeling of interphase turbulent kinetic energy transfer in particle-laden turbulent flows. *Phys. Fluids* **19** (8), 085101.

XU, Y. & SUBRAMANIAM, S. 2010 Effect of particle clusters on carrier flow turbulence: A direct numerical simulation study. *Flow Turbul. Combust.* **85**, 735–761.

YEUNG, P. K. & POPE, S. B. 1988 An algorithm for tracking fluid particles in numerical simulations of homogeneous turbulence. *J. Comput. Phys.* **79** (2), 373–416.

ZHANG, Z. & PROSPERETTI, A. 2005 A second–order method for three–dimensional particle simulation. *J. Comput. Phys.* **210** (1), 292–324.

ZICK, A. A. & HOMSY, G. M. 1982 Stokes flow through periodic arrays of spheres. *J. Fluid Mech.* **115**, 13–26.